The following publication Zou, K., Dan, Y., Xu, H., Zhang, Q., Lu, Y., Huang, H., & He, Y. (2019). Recent advances in lead-free dielectric materials for energy storage. Materials Research Bulletin, 113, 190-201 is available at https://doi.org/10.1016/j.materresbull.2019.02.002.

Recent advances in lead-free dielectric materials for energy storage

Abstract

With rapid development of the electronic and electrical industry, the demand for dielectric capacitors with ultrahigh power density（on the order of GW/kg）and energy conversion efficiency (＞90%) is continuously growing. Thus, it is imperative to present a timely review on the development of energy storage properties of dielectric capacitors. Unfortunately, existing reviews are mainly on lead-based dielectric capacitors. To reduce the environmental impact, lead-free dielectric capacitors must be the future development trend and many good research results have already been emerged. To better promote the development of this area, in this paper, we present a comprehensive review on the latest research progress of several mainstream lead-free dielectric materials, including ceramics (ferroelectrics/relaxor ferroelectrics/antiferroelectrics), glass-ceramics, thin/thick films and polymer-based composites, for energy storage applications, and point out their advantages and drawbacks. It is found that, in principle, lead-free dielectric materials with large saturation polarization, large breakdown electric field, small remnant polarization, and slim *P-E* loops are more appropriate for developing capacitors with high power density and high efficiency. Furthermore, some prospects based on current research work are proposed to propel lead-free dielectric capacitors to better meet newly emerging applications.

A table of contents should be added here.

1. Introduction

In recent years, with the evolution of economy and society, fossil energy crisis, climate change and air pollution have inspired massive efforts to explore clean and renewable energy resources, such as solar, water, wind and thermal energies. This leads to a high demand for energy storage systems, such as batteries, fuel cells, electrochemical supercapacitors, and dielectric parallel-plate capacitors[1-2]. Among them, batteries and fuel cells possess high energy density (200-1000 W·h/kg, and 10-300 W·h/kg, respectively), but their power densities are quite low (typically below 500 W/kg) because of the slow movement of charge carriers, which limits their applications in many high-power systems[3]. Electrochemical supercapacitors can offer high power density (10^1 to 10^6 W/kg) and moderate energy density (0.04 to 30 W·h/kg), while their charge/discharge processes are still long (seconds or even tens of seconds). In contrast, dielectric capacitors have faster charge/discharge rate (~ns), and much higher power density (up to 10^8 W/kg), which can well meet the requirement of super-high-power electronics and systems, such as hybrid electric vehicles, medical defibrillators, spacecraft, satellites, and electrical weapon systems. Table 1 summarizes the comparison between the electrochemical supercapacitor and the dielectric capacitor[3]. However, potential applications of dielectric capacitors are severely limited by their low energy density which is at least an order of magnitude lower than that of batteries, fuel cells and electrochemical capacitors, as shown in Fig. 1. It was reported that dielectric capacitors contribute more than 25% of the volume

and weight to power electronics and pulsed power systems[4]. Thus, it is urgent to develop novel dielectric materials that can significantly increase the energy density of the dielectric capacitors. In order to achieve this objective, much attention have been paid to lead lanthanum zirconate titanate (PLZT), lead lanthanum zirconate stannate titanate (PLZST), and lead magnesium niobate-lead titanate (PMN-PT), etc., since they show higher energy densities than other dielectric materials[5-7]. Nevertheless, the use of lead-based materials can seriously pollute the environment and endanger human health[8-11]. Therefore, it's necessary to search alternative lead-free dielectric materials with excellent energy storage properties. Although many relevant works have been reported, up to now, there is no comprehensive review on the current status of research in lead-free dielectric materials for energy storage applications.

In view of this, in this paper, we focus on the recent progress of various kinds of lead-free dielectric materials (including ceramics, thin/thick films and polymer-based composites) for energy storage applications. Their energy storage principles and properties will be compared and analyzed in order to provide guidance to the searching of new lead-free materials and the design of novel dielectric capacitors with high energy density, high power density and high energy storage efficiency. Future prospects are also proposed for the further investigation and optimization of dielectric capacitors.

Table 1. Comparison between electrochemical capacitors and nonlinear dielectric capacitors.

Electrochemical supercapacitor	Nonlinear dielectric capacitor
Use of liquid electrolytes	Use of solid dielectric material
Large capacitance (~10 000 F)	Small capacitance (<0.01 F)
Low maximum voltage (<3 V)	High maximum voltage (>300 V)
Slow charge/discharge (~s)	Fast charge/discharge (~μs to ms)
Medium power output (10^1 to 10^6 W/kg)	High power output (~10^8 W/kg)
Medium cycling life (~100 000)	Long cycling life (almost unlimited)
High leakage current (~mA)	Low leakage (~0.1 mA)
Not easy to fabricate	Easy to fabricate
Medium energy density (0.04 to 30 W·h/kg)	Low to medium energy density (see

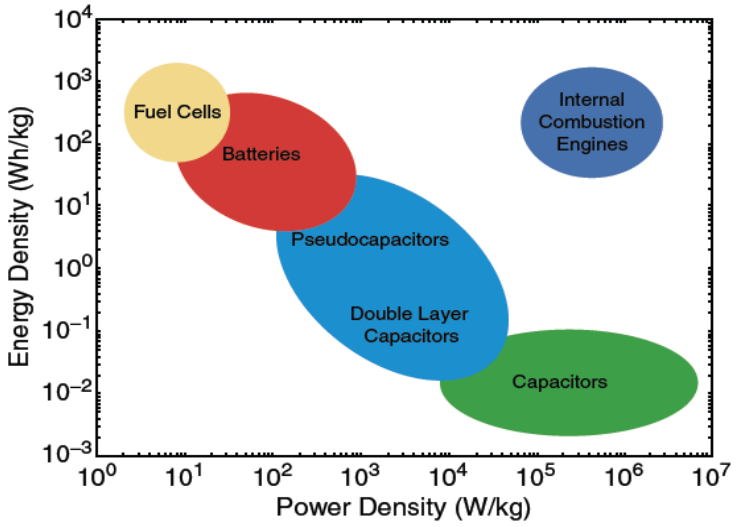

Fig. 1. Diagram of power density and energy density for various energy storage devices.

2. Principles and Measurement of Energy Storage in Dielectric Capacitors

A typical dielectric capacitor consists of two electrode plates filled with dielectric materials, as shown in Fig. 2. The capacitance, which measures the energy-storage capability of capacitors, can be calculated by the Eq. (1):

$$C = \varepsilon_0 \varepsilon_r \frac{A}{d} \tag{1}$$

where C is the capacitance, ε_0 is the vacuum permittivity, ε_r is the relative permittivity

(dielectric constant), A is the overlapped area of two plates and d is the distance between the plates. When an external electric field is applied during the charging process, the dipoles inside the dielectric material will be re-oriented along the direction of the electric field and induced charges will be produced on two plates. The charging process is over when the potential difference generated by the accumulated charges ($\pm Q$) is equal to the external voltage and the electrostatic field energy is be stored in the capacitor. The

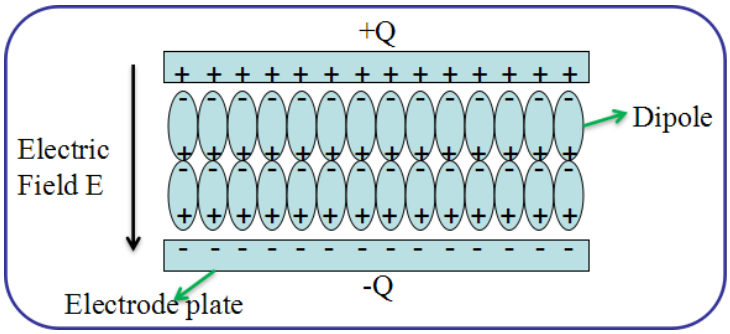

Fig. 2. The diagram of dielectric polarization during the charging process.

capacitance, C, can be also defined in a differential form of the change of charge with respect to voltage:

$$C = \frac{\mathrm{d}Q}{dV} \tag{2}$$

During the charging process, the total stored energy W can be given as:

$$W = \int_0^{\mathrm{Q}} \mathrm{V}\mathrm{d}q\,. \tag{3}$$

and thus the energy storage density (J), which is defined as the energy stored per unit volume of dielectric, can be expressed as,

$$J = \frac{W}{Ad} = \frac{\int_0^{Q_{\max}} Vdq}{Ad} = \frac{\int_0^{\delta_{\max}} Vd\delta}{d} = \int_0^{D_{\max}} EdD \tag{4}$$

where E is the external electric field applied on dielectric materials and equal to V/d,

δ is the surface charge density, D is the electrical displacement ($D=\delta$, according to Maxwell equations). For dielectric capacitors, energy storage density, J, is a very important parameter. Large J favors the miniaturization, lightweight and integration of electronic devices. For linear dielectric (LD) materials (e.g., mica, glass, and diamond-like carbon films), their dielectric constant remains constant when the applied electric field E changes, as presented in Fig. 3(a), and thus, the J can be simply calculated as:

$$J = \int_0^{D_{\max}} EdD = \int_0^{E_{\max}} Ed\varepsilon_0\varepsilon_r E = \frac{1}{2}\varepsilon_0\varepsilon_r E^2 \qquad (5)$$

From this equation, it can be found that the energy storage density is directly proportional to the relative permittivity and the square of the applied electric field. However, the Eq. (5) is not suitable for nonlinear dielectric materials because of the variation of dielectric constant with electric field, as displayed in Fig. 3(b). When dielectric constants of the dielectric materials are large, the electrical displacement is very close to the polarization. Thus, the Eq. (4) can be expressed as:

$$J = \int_0^{P\text{sat}} \mathrm{E}dP \qquad (6)$$

where P and P_{sat} are spontaneous and saturation polarizations, respectively. Eq. (6) demonstrates that the energy storage density of a dielectric material is equal to the area enclosed by the vertical axis and the hysteresis loop during charging process (sum of the blue and red areas), as shown in Fig. 4. Fig. 4(a), (b), (c), and (d) exhibit polarization-electric field (P-E) hysteresis loops for linear dielectrics (e.g., Al_2O_3), ferroelectrics (FE, e.g., $PbZr_xTi_{1-x}O_3$), relaxor ferroelectrics (RFE, e.g., xPb($Mg_{1/3}Nb_{2/3}$)O_3-(1-x)$PbTiO_3$) and antiferroelectrics (AFE, e.g., $PbZrO_3$) respectively. As illustrated in Fig. 4, during discharging process, not all stored energy can be released due to the energy loss (J_{loss}, red area) induced by the electric

hysteresis. The recoverable energy storage density (J_{rec}, blue area), which is equal to the area enclosed by the vertical axis and the hysteresis loops during discharging process, and the energy storage efficiency (η) can be expressed as:

$$J_{rec} = -\int_{P_{sat}}^{P_r} EdP \text{ (upon discharging)} \quad (7)$$

$$\eta = \frac{J_{rec}}{J_{rec} + J_{loss}}. \quad (8)$$

As seen from Fig. 4, and the Eq. (7), high electric field breakdown strength(BDS), large saturated polarization, small remnant polarization and slim *P-E* loop are very helpful for obtaining high J_{rec} and η. Although linear dielectric usually have higher breakdown electric field and lower energy loss, their small saturated polarizations (proportional to dielectric constants) make them not applicable for high energy-storage application. Thus, in this work, we mainly focus on the research progress on nonlinear lead-free ferroelectric, relaxor ferroelectric, and antiferroelectric materials (including ceramics, thin/thick film, and polymer) for energy storage applications.

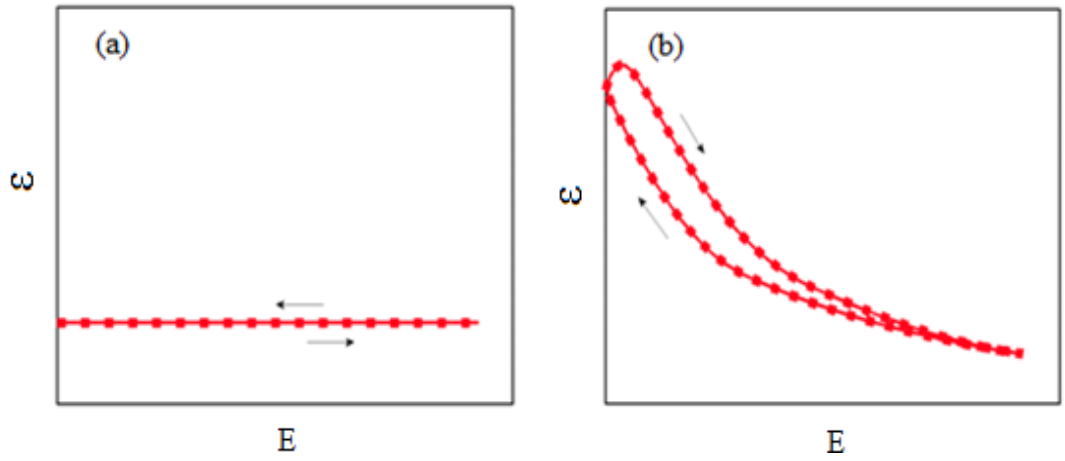

Fig. 3. Dielectric constant as a function of applied electric field for (a) linear dielectric, and (b) nonlinear dielectric (e.g., ferroelectrics).

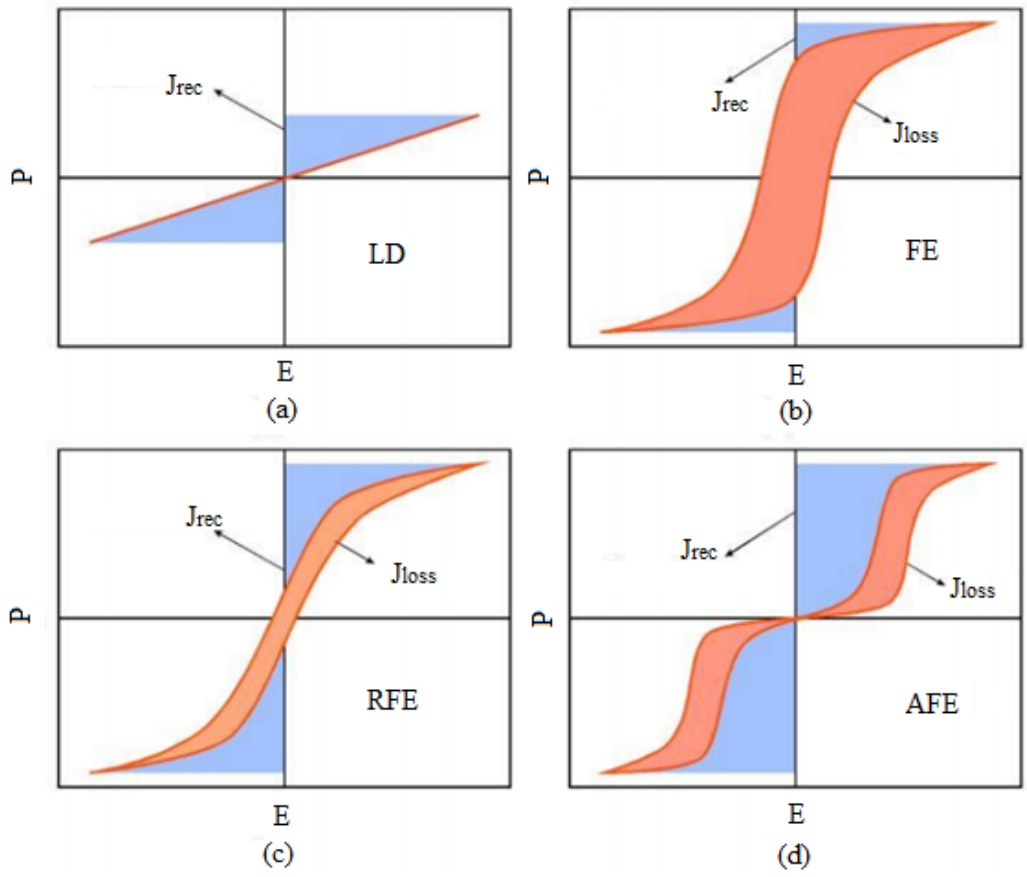

Fig. 4. Diagram of *P-E* hysteresis loops for (a) linear dielectrics, (b)ferroelectrics, (c) relaxor ferroelectrics, (d) antiferroelectrics and some characteristic parameters for energy storage.

The J_{res} can be calculated not only by quasi-static *P-E* hysteresis loop, but also by dynamic pulsed discharge current, as shown in Fig. 5. In the charging process, the switch 1 is connected to the switch 3 and electric energy can be stored in dielectric materials. When this process is finished, the switch 1 is quickly changed to the switch 2 and meanwhile, the discharging process begins. On the basis of circuit theory, the J_{res} can be also expressed as[12]:

$$J_{res} = \frac{R\int i^2(t)dt}{V} \tag{9}$$

where R, i(t), t, and V are the resistance of the resistor in the circuit, the discharge current, the discharge time, and the volume of the dielectric capacitor, respectively. In FE or AFE state, the dynamic result is generally smaller than the quasi-static result, as illustrated in Fig. 6 and until now, there has been still no reasonable explanation on the remarkable difference[12].

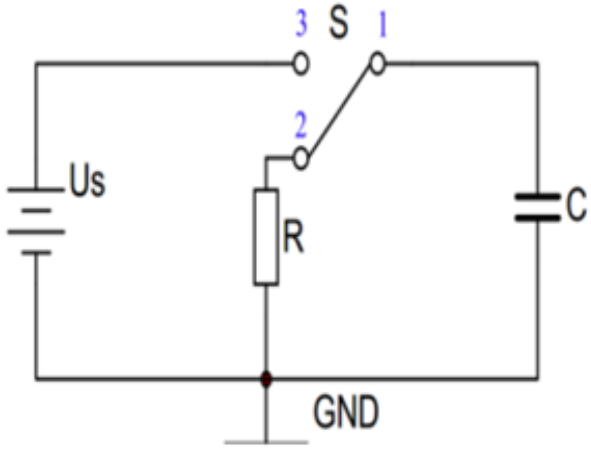

Fig. 5. The circuit used to measure the discharging current.

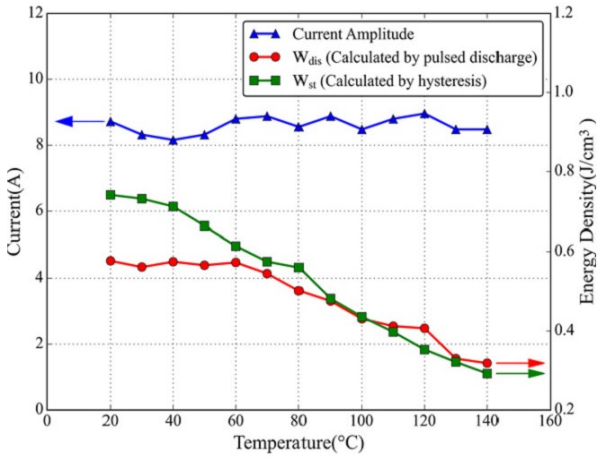

Fig. 6. Current amplitude and released energy density calculated by quasi-static hysteresis loop and pulsed discharge.

3. Energy-Storage Properties in Lead-Free Dielectric Materials

3.1. Energy-storage in lead-free ferroelectrics ceramics

FE materials possess spontaneous polarization in a certain temperature range even if there is no external electric field. Above the Curie temperature, the spontaneous polarization disappears and the ferroelectric phase transforms to non-ferroelectric phase (paraelectric phase), where the material exhibits a linear dielectric behavior. In this section, we only discuss energy storage properties of FE materials in the FE state.

As a kind of typical room-temperature ferroelectric material, barium titanate ($BaTiO_3$) possesses high saturation polarization which is beneficial to high energy storage density. However, its large remnant polarization results in small energy conversion efficiency of $BaTiO_3$ capacitor and the energy loss will produce heat and affect the service life of device. Doping is a feasible way to tailor the energy storage performance of ferroelectric materials. The substitution for Ba^{2+} or Ti^{4+} with equivalent or hetero valent ions can result in significant improvement in the energy-storage properties[13]. Doping of Ca^{2+} (or Sr^{2+}) and Zr^{4+} to replace Ba^{2+} and Ti^{4+}, respectively, usually results in lower remnant polarization and energy loss, and higher energy density and efficiency. For example, a relatively large recoverable energy density of 1.41 J/cm^3, about 40% higher than that of pure $BaTiO_3$, and a moderate energy efficiency of 61% were obtained in $Ba_{0.70}Ca_{0.30}TiO_3$ (BCT) bulk ceramic. Compared with pure $BaTiO_3$, BCT bulk ceramics exhibit lower remnant polarization, energy loss and more slim *P-E* hysteresis loop[14]. When Zr^{4+} ions are doped into the $BaTiO_3$ lattice, they usually replace Ti^{4+} ions because of similar ionic radius. Since Zr^{4+} has a fixed valence state in comparison with multi-valence state of

Ti (Ti^{4+} and Ti^{3+}), the doping of Zr^{4+} can reduce the electron hopping conduction between Ti^{4+} and Ti^{3+}, suppressing the energy loss[15-18]. Zhang *et al*. found that, by selecting appropriate sintering temperature, excellent dielectric and energy storage properties (dielectric constant of 2998, dielectric loss of 0.007 and energy storage density of 0.5 J/cm^3) can achieved in Zr^{4+} doped $BaTiO_3$ ($BaZr_{0.1}Ti_{0.9}O_3$) ceramics[19]. Moreover, $[(BaZr_{0.2}Ti_{0.8})O_3]_{1-x}$-$[(Ba_{0.7}Ca_{0.3})TiO_3]_x$ (x=0.10, 0.15, 0.20) (BZT-BCT) ceramics prepared by sol-gel synthesis technique show improveed energy storage capacity. All compositions studied display slim *P-E* loops (Fig. 7) and energy storage densities of 0.60, 0.25, and 0.05 J/cm^3 for samples with x=0.10, 0.15, and 0.20, respectively[20].

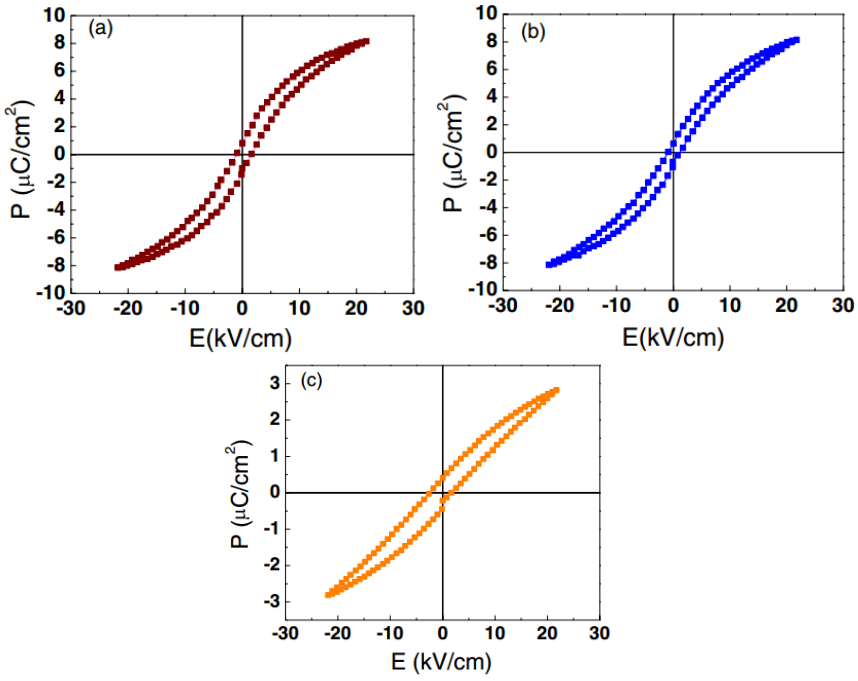

Fig. 7. Room-temperature *P-E* curves of sol-gel derived $[(BaZr_{0.2}Ti_{0.8})O_3]_{1-x}$-$[(Ba_{0.7}Ca_{0.3})TiO_3]_x$ (x = 0.10, 0.15, and 0.20) ceramics measured at 50Hz.

As shown in the Fig. 4, in addition to the low remnant polarization and large saturation polarization, high BDS is also the key to high energy-storage performance

of ferroelectric ceramics. To realize high BDS value, FE ceramics with high quality (few porosity, fine and uniform grain size) are demanded. Surface modification of ceramic particles is demonstrated to be a promising method to obtain ceramics with high energy storage density. The BDS of $BaTiO_3$ (BT) ceramics was obviously improved by coating the Al_2O_3 or B_2O_3-SiO_2 thin layer on the surface of BT ceramic particles. Fig. 8 illustrates that, compared with unmodified BT ceramic, the BDS values and energy storage densities of Al_2O_3-doped BT (BT@A) and B_2O_3-SiO_2-doped BT (BT@G) ceramics were greatly improved. Their energy storage densities were as high as 2.5 and 3.2 J/cm^3, respectively. The enhanced BDS values for BT@A and BT@G ceramics were attributed to the prominent reduction in the pore defects, and the electron blocking by Al_2O_3 and B_2O_3-SiO_2 layers, respectively[21]. Wu *et al*. prepared $Ba_{0.3}Sr_{0.7}TiO_3$ (BST) ceramics by conventional sintering (CS) and spark plasma sintering (SPS) methods. As can be seen in Fig. 9, SPS samples exhibited much smaller grain sizes, less porosities and fewer defects, which resulted in reduced dielectric loss (0.0025), enhanced BDS and improved energy storage density[22]. Moreover, the effect of sintering atmosphere (N_2, air and O_2) on the energy storage performance of BST ceramics was studied by Jin *et al*[23]. who found that the grain size of the BST ceramics sintered in O_2 atmosphere could be reduced to 0.44 μm because the lack of oxygen vacancies inhibited the grain growth. As a result, a large BDS of 16.72 kV/mm, a high energy storage density of 1.081 J/cm^3 and a moderate energy storage efficiency of 73.78% were obtained.

Similar to $BaTiO_3$, strontium titanate ($SrTiO_3$) possesses ABO_3-type perovskite

structure. Cubic-structured $SrTiO_3$ possesses no spontaneous polarization and exhibits paraelectric phase[24]. Theoretically, paraelectric $SrTiO_3$ ceramics show a linear dielectric behavior. However, it was reported that $SrTiO_3$ in bulk form experimentally exhibited nonlinear dielectric behavior with *P-E* hysteresis loops[25]. The energy storage capacity of $SrTiO_3$ bulk ceramic is closely related to the shape of the *P-E* hysteresis loop and the BDS value. Yao *et al*. fabricated Mg-doped $SrTiO_3$ ($Sr_{1-x}Mg_xTiO_3$) ceramics by solid-state reaction method[26], whose BDS value was improved and the *P-E* loops became more slim with the addition of Mg (Fig. 10) due to reduced grain size and increased width of grain boundary. The ceramics exhibited interesting energy storage density of 1.86 J/cm^3 and high energy efficiency of 89.3%.

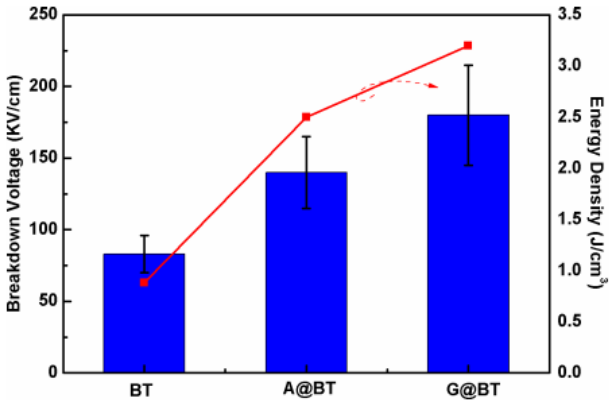

Fig. 8. Dielectric breakdown strength and the energy storage density of the BT, BT@A, and BT@G ceramics.

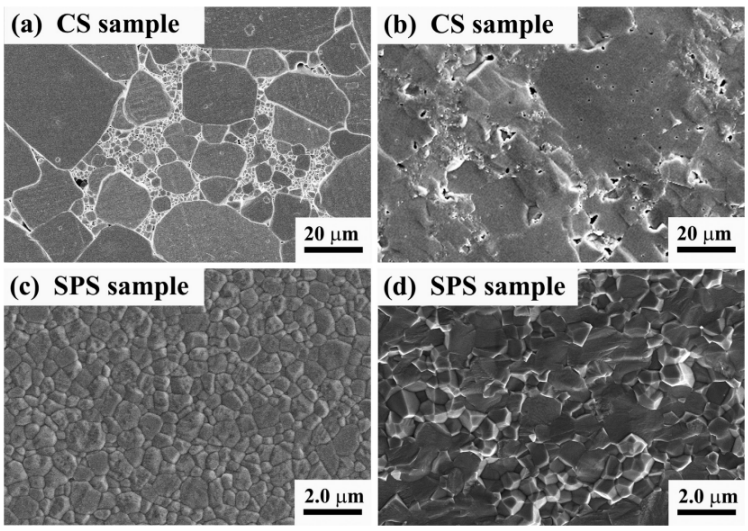

Fig. 9. SEM micrographs on polished and thermal-etched surfaces of BST ceramics prepared by (a) conventional sintering and (c) spark plasma sintering. Fracture surface of BST ceramics prepared by (b) conventional sintering and (d) spark plasma sintering.

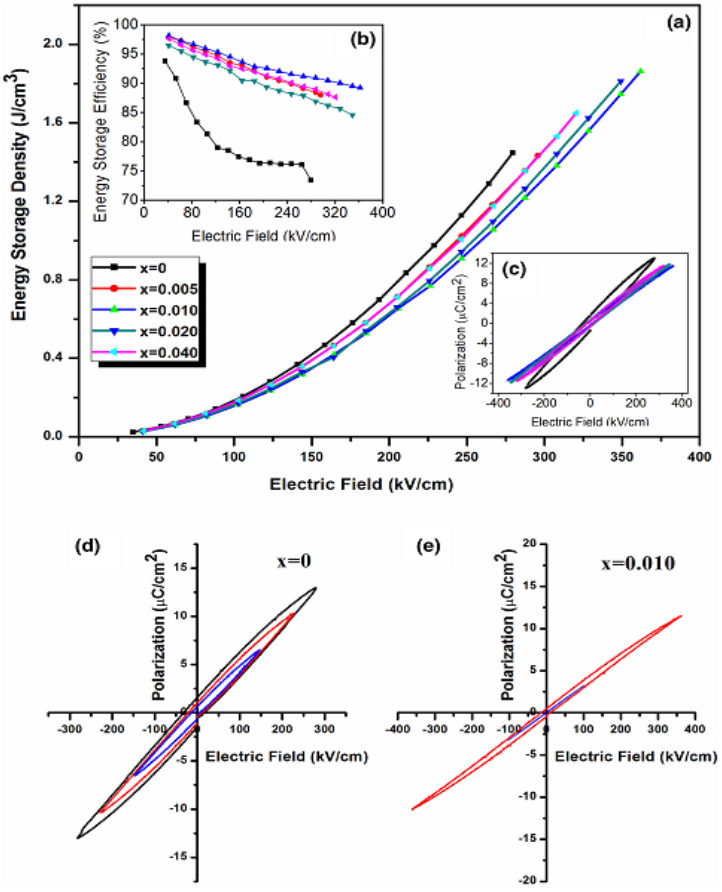

Fig. 10. The electric field dependence of (a) discharge energy storage density, (b)

energy storage efficiency and (c) polarization for $Sr_{1-x}Mg_xTiO_3$ ceramics. (d, e) Hysteresis loops of $SrTiO_3$ and $Sr_{0.99}Mg_{0.01}TiO_3$ ceramics, respectively.

$Bi_{0.5}Na_{0.5}TiO_3$(BNT) is another kind of widely studied ferroelectric materials, which possesses saturation polarization of ~43 μC/cm^2, attractive for energy storage[27]. However, high remnant polarization (~39 μC /cm^2), and large leakage current limit its application in energy storage[27]. To eliminate this unfavorable factor, numerous BNT-based solid solutions have been developed. Chandrasekhar *et al*. studied 0.93BNT-0.07BT (BNT-BT) and 0.93BNT-0.06BT-0.01$K_{0.5}Na_{0.5}NbO_3$ (KNN) ceramics and found that introducing KNN into BNT-BT system could significantly decrease the remnant polarization and the coercive field, leading to higher energy storage density of ~0.598J/cm^3 for the BNT-BT-KNN ceramics (~0.485J/cm^3 for the BNT-BT ceramics) [28].

3.2. Energy-storage in lead-free relaxor ferroelectric ceramics

Relaxor ferroelectrics (e.g., $PbMg_{1/3}Nb_{2/3}O_3$, $PbZn_{1/3}Nb_{2/3}O_3$, $PbSc_{1/2}Nb_{1/2}O_3$, (1-x)$SrTiO_3$-x($Na_{0.5}Bi_{0.5}$)TiO_3，and (1-x)$BaTiO_3$-x$Bi(Zn_{0.5}Ti_{0.5})O_3$)) are thought to be dipolar glasses displaying a lack of long-range ordered structure such as ferroelectric domains[29]. Hence, compared with ferroelectric materials, they exhibit near-zero remnant polarization and more slim *P-E* loops (Fig. 4(c))，leading to high energy efficiency. Particularly, the polarization of relaxor ferroelectrics can exhibit a good temperature stability because of their diffuse phase transition behavior around the dielectric maxima[30].

Among lead-free relaxor ferroelectric ceramics, $BaTiO_3$(BT)-based materials have recently received increasing attention for energy storage applications because of their good ferroelectric and dielectric properties. Introduction of other elements into A- or B-site of BT will result in the appearance of ferroelectric relaxor behavior[31-33]. Wei *et al*. doped $BiYO_3$ into BT and obtained an energy storage density of 0.316 J/cm^3 with an energy efficiency of 82.7% in $0.8BaTiO_3$-$0.2BiYO_3$ relaxor ferroelectric ceramic. With increasing $BiYO_3$ content, the classic ferroelectric behavior in pure $BaTiO_3$ gradually transforms into highly diffusive and dispersive relaxor characteristics. Thus, the *P-E* loops became more and more slim, resulting in higher and higher energy efficiency, as shown in Fig. 11[34]. By introducing $Bi(Mg_{2/3}Nb_{1/3})O_3$ (BMN)

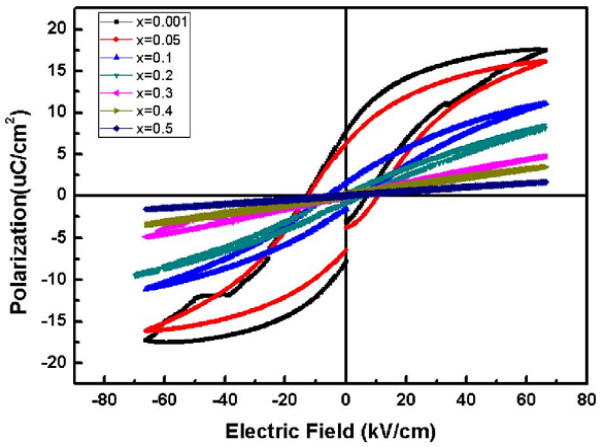

Fig. 11. Room temperature P-E hysteresis loops for (1-x)$BaTiO_3$ -x$BiYO_3$ ceramics (x=0.001, 0.05, 0.1, 0.2, 0.3, 0.4, and 0.5) measured at 10 Hz

into BT, a relaxor-like feature was obtained in BT-BMN ceramics, with increased energy density. The maximum BDS and energy density could reach 287.7 kV/cm and 1.13 J/cm^3, respectively[35]. Similarly, the solid solution of 5-20 mol% $Bi(Zn_{2/3}Nb_{1/3})O_3$ (BZN) and $BaTiO_3$ showed obvious relaxor character. With

increasing BZN content, the permittivity peaks became rather broadened and flattened with more slim *P-E* loops (Fig. 12). The optimal discharge energy density of 0.79 J/cm^3 and a high efficiency of 93.5% were achieved at 131 kV/cm for the sample with 15 mol% of BZN[36]. Dong *et al*. found that the introduction of $Bi(Zn_{0.5}Ti_{0.5})O_3$ could not only increase the relaxor degree of $BaTiO_3$ materials but

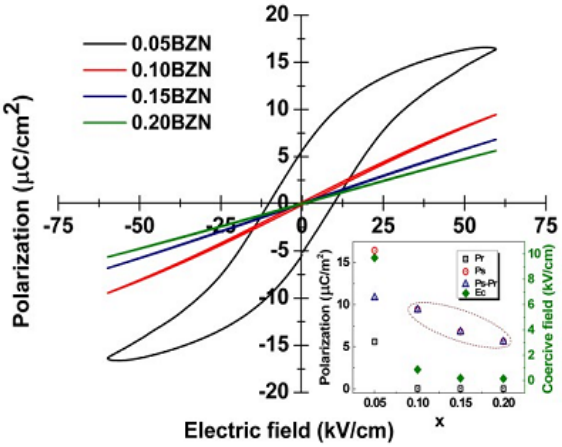

Fig. 12. P-E hysteresis loops of various BT-BZN ceramics. The inset shows the composition dependent P_r, E_s, P_s-P_r and E_c.

also improve the temperature stability. When the content of $Bi(Zn_{0.5}Ti_{0.5})O_3$ was 14 mol%, at 25℃, 50℃, 100℃, 150℃ and 180℃, the discharge energy density were nearly the same and could reach 0.81, 0.80, 0.78, 0.72, and 0.67 J/cm^3, respectively[37]. Superior energy storage performance can be obtained by introducing transition metal element into the BT based relaxor solid solution. For example, $0.9BaTiO_3$-$0.1Bi(Mg_{2/3}Nb_{1/3})O_3$-0.3wt.%$MnCO_3$ ceramics showed a recoverable energy density of about 1.70 J/cm^3 with an efficiency of about 90% under an electric field of 210 kV/cm, due to increased BDS value (Fig. 13)[38]. Recently,

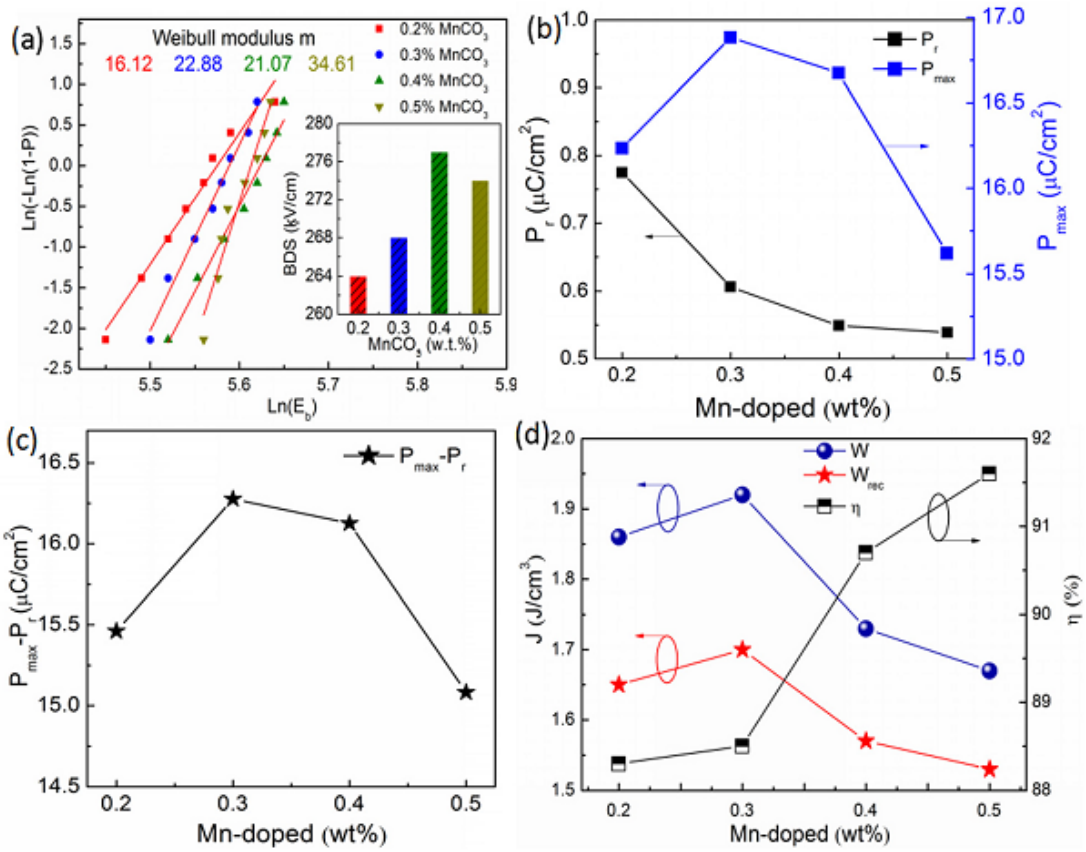

Fig. 13. (a) Weibull distributions and the fitting lines of the BDS. (b) P_{max}, P_r, and (c) P_{max}-P_r values measured at the same applied electric field of 150 kV/cm. (d) Energy storage density and efficiency of $0.9BaTiO_3$-$0.1Bi(Mg_{2/3}Nb_{1/3})O_3$-x wt.% $MnCO_3$ ($0.2 \leqslant x \leqslant 0.5$) ceramics measured at their BDS.

energy storage properties of some other systems (e.g., $BiFeO_3$, $SrTiO_3$, $Bi_{0.5}Na_{0.5}TiO_3$, and $K_{0.5}Na_{0.5}NbO_3$) have also been studied. $BiFeO_3$ (BF) is recognized as a good ferroelectric material due to its large intrinsic polarization (P_{sat} >100μC/cm^2). However, pure BF is not suitable for the energy storage application owing to its high leakage current. In order to solve this problem, doping of various kinds of materials into BF has been tried. For example, BF doped with BT possessed a high P_{max}, but their energy storage density was low because of the large energy loss and high P_r value[39]. $(0.67\text{-}x)BiFeO_3$-$0.33BaTiO_3$-$xLa(Mg_{1/2}Ti_{1/2})O_3$ ternary lead-free ceramics

exhibited an obvious dielectric relaxation behavior[40]. A good energy storage density of 1.66 J/cm^3 at 13kV/mm and a relatively high energy efficiency of 82% were achieved in the ceramics with x=0.06, as shown in Fig. 14. Besides, the energy storage properties of the ceramics not only depend weakly on frequency (0.2 -100 Hz), but also exhibited a good stability against temperature (25-180℃), as presented in Fig. 15. These properties were attributed to a rapid response of the electric field induced reversible ergodic relaxor to long-range ferroelectric phase transition and a typical diffuse phase transformation process near the dielectric maxima. An excellent energy storage density of 1.56 J/cm^3 and a moderate energy efficiency of about 75% were also obtained in $0.61BiFeO_3$-$0.33BaTiO_3$-$0.06Ba(Mg_{1/3}Nb_{2/3})O_3$ lead-free relaxor ferroelectric ceramic, with good temperature stability in the temperature range of 25 to 190℃[41].

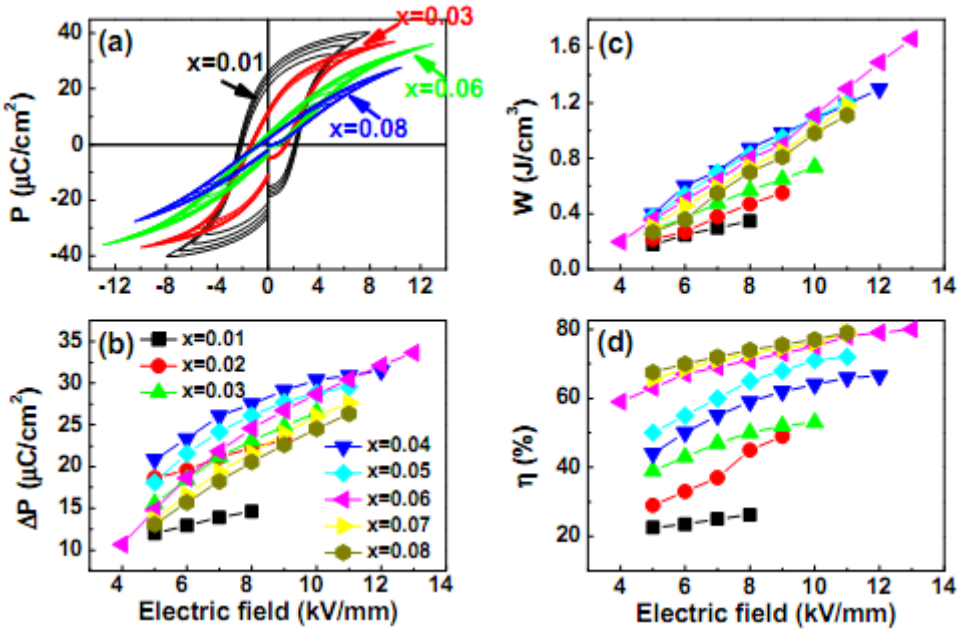

Fig. 14. (a) *P-E* loops measured under different electric fields at 1 Hz for a few representative compositions, and (b) $\triangle P = P_{max}-P_r$, (c) energy storage density *W*

and (d) energy storage efficiency η of (0.67-x)BF-0.33BT-xLMT ceramics varying with the magnitude of the applied electric field.

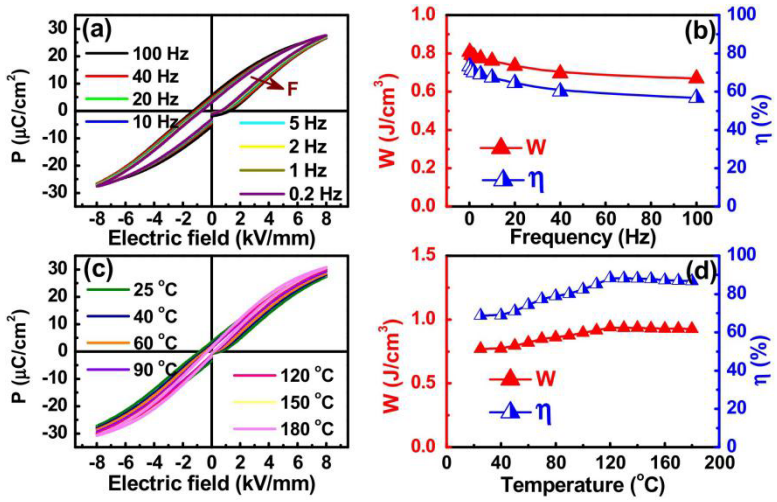

Fig. 15. (a) *P-E* loops of the x=0.06 ceramic sample measured at room temperature in the frequency range of 0.2-100 Hz, and (b) the calculated *W* and η values as a function of frequency; (c) *P-E* loops of the x=0.06 ceramic sample measured at room temperature at 1 Hz in the temperature range of 25-180 ℃, and (d) the calculated *W* and η values as a function of temperature.

It has been confirmed that cubic $SrTiO_3$ (ST) can form solid solution with lots of ferroelectrics (such as $BaTiO_3$, $Bi_{0.5}Na_{0.5}TiO_3$, $K_{0.5}Na_{0.5}NbO_3$) and show relaxor characters[42-44]. For instance, (1-x)$SrTiO_3$-x($Na_{0.5}Bi_{0.5}$)TiO_3 ceramics showed broad relaxor behavior due to increased degree of lattice disorder and thus exhibited a high energy conversion efficiency. Particularly, the discharge energy density was improved obviously because of the enhancement of P_m [45], as presented in Table 2. For ternary system, when x=0.3, (1-x)$SrTiO_3$-x(0.65$BaTiO_3$ -0.35$Bi_{0.5}Na_{0.5}TiO_3$) relaxor ceramics possess not only an energy storage efficiency of more than 90%, but also a high energy storage density of 1.40 J/cm^3 because of the large P_{sat} [46].

Table 2. E_b, P_m, J_d, J_c and η of (1-x)ST-xNBT ceramics at room temperature.

Composition	$x = 0.1$	$x = 0.2$	$x = 0.3$	$x = 0.4$	$x = 0.5$	$x = 0.6$
E_b (kV/mm)	25.96	23.95	21.00	20.98	17.97	13.89
P_m (μC/cm^2)	13.78	18.64	23.65	25.37	34.21	30.78
J_d (J/cm^3)	1.24	1.58	1.65	1.70	1.35	1.18
J_c (J/cm^3)	1.87	2.25	2.43	2.54	3.51	2.33
η (%)	66.31	70.22	67.90	69.93	38.46	50.64

For $K_{0.5}Na_{0.5}NbO_3$ system, it has been found that the addition of the secondary compound can tune the grain size of KNN-based ceramics to submicrometer and improve the relaxor character. For instance, the grain size was decreased from 4-8 μm for pure KNN ceramics to 0.5 μm for 0.8KNN-0.2Sr($Sc_{0.5}Nb_{0.5}$)O_3 and the *P*-*E* loop was more slim[47]. Due to the dense microstructure, submicron grain size and decreased P_r, 0.8KNN- 0.2Sr($Sc_{0.5}Nb_{0.5}$)O_3 ceramics displayed large energy storage density (2.48 J/cm^3 under an electric field of 295 kV/cm). Yang *et al*. successfully fabricated 0.85KNN-0.15$SrTiO_3$ relaxor ferroelectric ceramics with submicrometer grains (about 0.3 μm) using pressureless solid state sintering and obtained a BDS of 400 kV/cm with a large energy storage density of 4.03 J/cm^3 (Fig. 16)[48]. The grain size of the KNN ceramics can also be significantly decreased by forming solid solution with Bi($Mg_{2/3}Nb_{1/3}$)O_3, resulting in the increase of P_{sat} and BDS, and the decrease of P_r, as shown in Figs. 17 and 18[49]. Finally, Large P_s (41 μC/cm^2) and high BDS (300 kV/cm) were obtained in 0.90KNN-0.10BMN ceramics, leading to a large energy storage density of 4.08 J/cm^3.

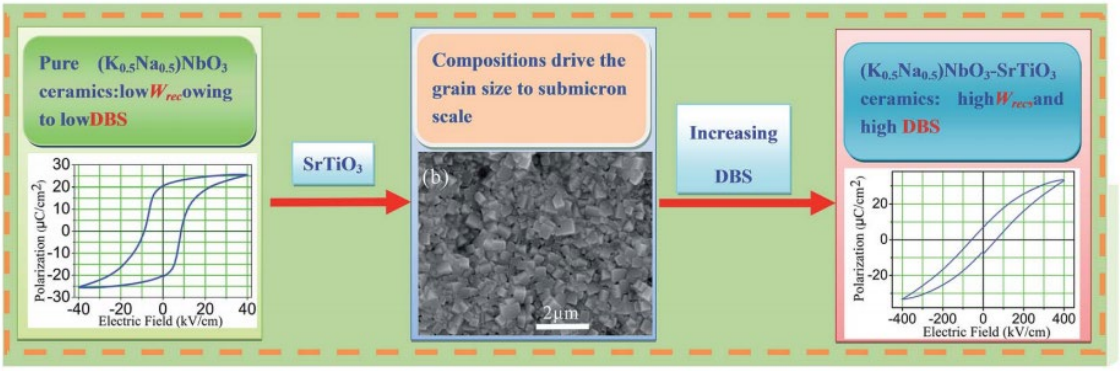

Fig. 16. Schematic diagram showing the increase of BDS and W_{rec} by decreasing the grain size to the submicron scale.

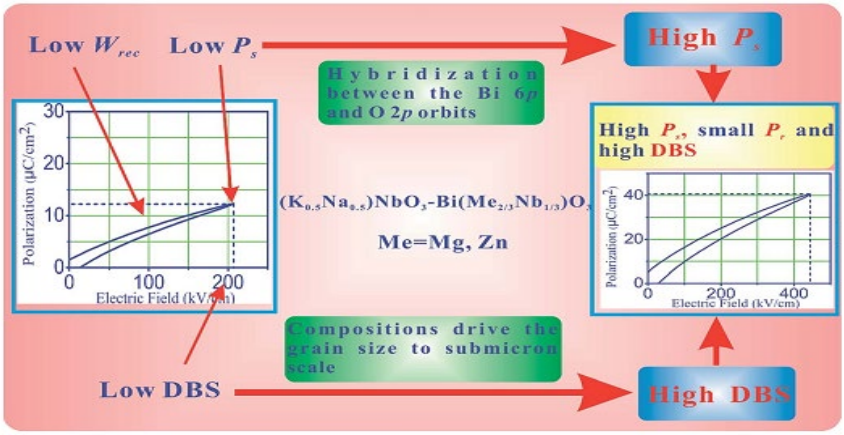

Fig. 17. Schematic diagram showing the increase in P_s, BDS, and W_{rec} through designing new KNN-based ceramics.

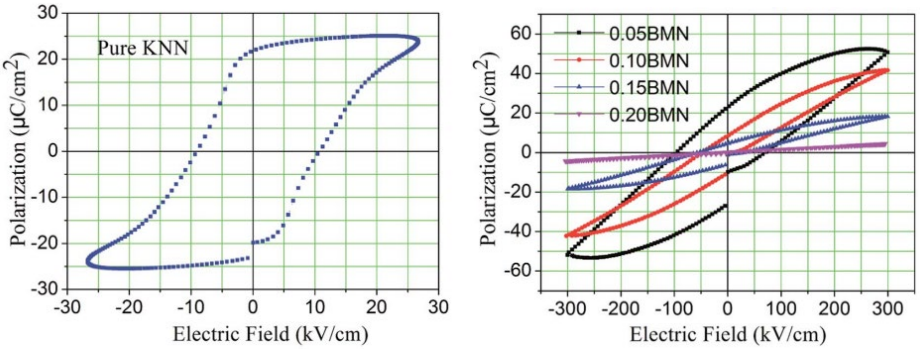

Fig. 18. *P-E* loops of (1-x)KNN-xBMN ceramics at selected applied electric fields.

Energy storage properties of $Bi_{0.5}Na_{0.5}TiO_3$ based lead-free relaxor ferroelectric ceramics have also been paid much attention. Li *et al*. synthesized $CaZrO_3$ (CZ)-doped 0.94BNT-0.06$BaTiO_3$ (BNBT6) ferroelectric ceramics using conventional

solid state reaction[50] and obtained the maximum energy storage density of 0.7 J/cm^3 under 70 kV/cm in 0.97BNBT6-0.03CZ, with stable energy storage property in the temperature range of 30-130℃. The introduction of CZ decreased the porosity of BNBT6 ceramics, and enhanced the relaxor character. Similarly, adding KNN into (1-y)BNT-yBKT ceramic disrupted the long range ferroelectric order, resulting in more slim *P-E* loops and enhanced energy storage properties. A maximum energy storage density of 1.20 J/cm^3 at 100 kV/cm was achieved in 0.16KNN-doped $Bi_{0.5}Na_{0.5}TiO_3$ ceramics, which exhibited fatigue-free behavior and temperature-independent characteristic due to the stable relaxor pseudocubic (antiferroelectric-like) phase over a wide temperature range[51]. Particularly, a higher energy storage density of 1.4 J/cm^3 was achieved in 0.85(0.94BNT-0.06BT)-0.15$Na_{0.73}Bi_{0.09}NbO_3$ ceramic, which was mainly attributed to the large saturation polarization P_m (30 μC/cm^2) and reduced remnant polarization P_r (5 μC/cm^2)[52].

3.3. Energy-storage in lead-free antiferroelectric ceramics

Unlike ferroelectrics which possess spontaneous polarization, the net polarization of antiferroelectrics is zero because of anti-parallel dipoles. Under a high enough applied electric field (AFE-FE phase switching field, E_F), the anti-parallel dipoles in AFE phase are aligned to form FE phase and macroscopic polarization can be induced, as shown in Fig. 19(a) [53]. When the external electric field decreases to the FE-AFE phase switching electric field (E_A), the FE phase will come back to AFE

phase again, as presented in Fig. 19(b). Therefore, antiferroelectrics show unique double *P-E* loops, as displayed in Fig. 20, which is expected to obtain high J_{rec} and η. It can be also seen from the figure that, in antiferroelectrics, the total energy density (J_{loss}+J_{rec}), J_{rec} and η are closely related to E_F, E_A and $\triangle E$ (E_F-E_A), respectively. The values of E_F and E_A can be obtained from the *I-E* curve, as shown in Fig. 21. When the applied electric field is positive, the positive current peak corresponds to E_F, whereas the negative current peak correlates to E_A[54]. Compared with ferroelectrics and relaxor ferroelectrics, except for higher J_{rec} and η, antiferroelectrics display faster discharging rate (ns) because of the sudden loss of FE phase at the switching electric field E_A[55-56].

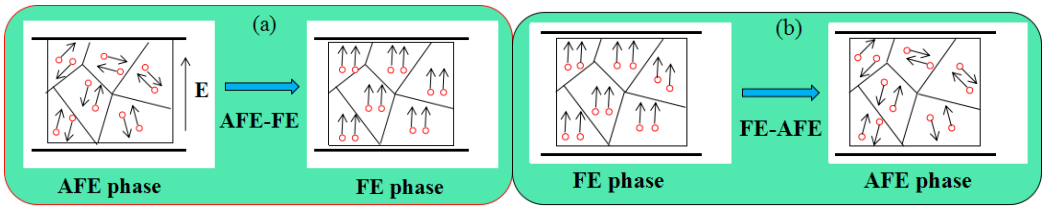

Fig. 19. (a) The reorientation of the electric dipoles in AFE under an external switching electric field E_F and (b) the reorientation of the electric dipoles after removing the external electric field.

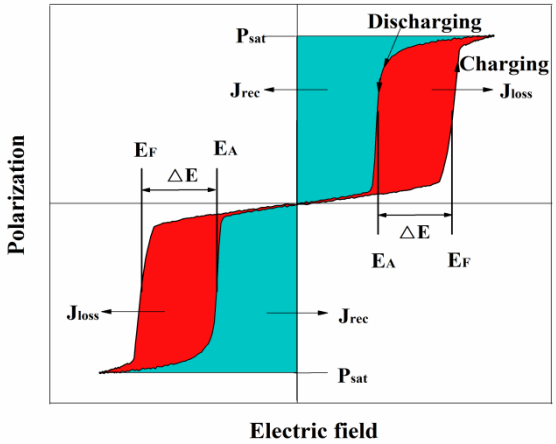

Fig. 20. Typical double *P-E* hysteresis loop of antiferroelectric materials.

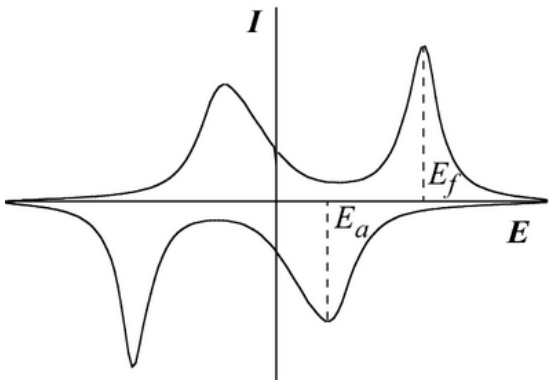

Fig. 21. Determination of the critical fields E_F and E_A in antiferroelectric materials from the current-electric field curve.

In the past few years, $PbZrO_3$-based antiferroelectrics have attracted much attention due to their high J_{rec} and high η[57-60]. In view of the toxicity of lead, the current research interest is gradually shifting to lead-free AFE materials, such as $(Bi_{0.5}Na_{0.5})TiO_3$ and $AgNbO_3$ systems.

Ding *et al*. found that $0.89Bi_{0.5}Na_{0.5}TiO_3$-$0.06BaTiO_3$- $0.05K_{0.5}Na_{0.5}NbO_3$ ceramics fabricated by two-step sintering showed more antiferroelectric-like behaviors than those prepared by single-step sintering (Fig. 22).[61]. The energy storage density of ceramics by two-step sintering is 0.9 J/cm^3, three times larger than that by single-step sintering. Later, the two-step sintering method was used to fabricate ST-doped BNT binary AFE ceramics, which showed low P_r (3.21 μC/cm^2), large P_{sat} (31.05 μC/cm^2), and high energy storage density (0.95 J/cm^3). With increasing ST content, the ceramics transformed from rhombohedral FE phase into the tetragonal AFE phase, as shown in Fig. 23[62]. Similarly, low P_r of 1.9μC/cm^2, and

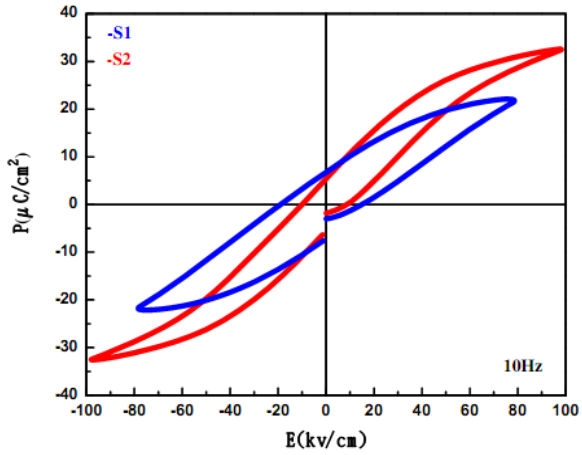

Fig. 22. The *P-E* loops of $0.89Bi_{0.5}Na_{0.5}TiO_3$-$0.06BaTiO_3$-$0.05K_{0.5}Na_{0.5}NbO_3$ ceramics by single-step (S1) and two-step (S2) sintering method

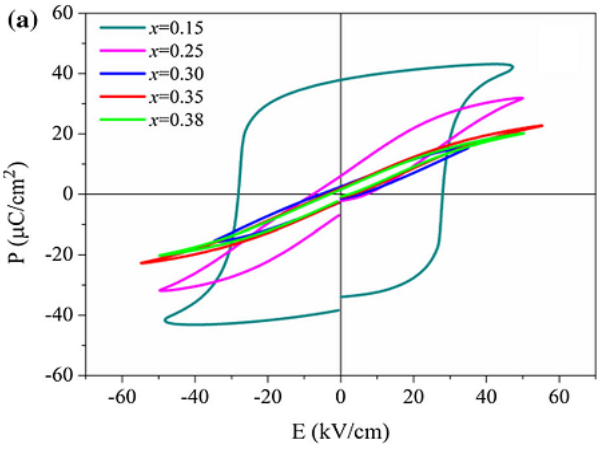

Fig. 23. The P-E hysteresis loops of BNT-xST ceramics

large J_{rec} of 0.97J/cm^3 was achieved in 25 mol% ST-doped 0.80BNT-0.20BKT ternary lead-free AFE ceramics using the two-step sintering method[63]. The introduction of ST with appropriate amount significantly decreased the P_r, resulting in the increase of the J_{rec}, as shown in Fig. 24.Enhanced energy storage density of 1.15 J/cm^3 and efficiency of 73.2%

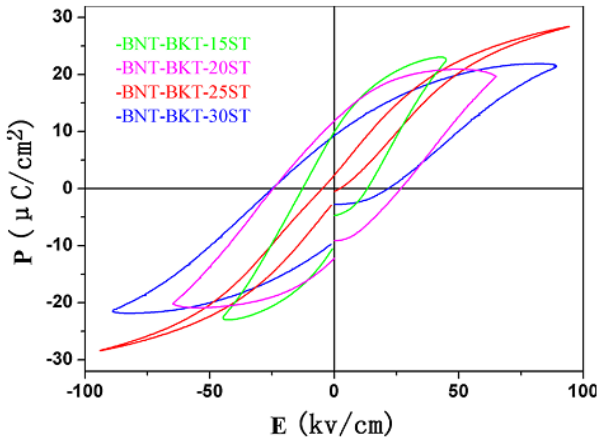

Fig. 24. *P-E* hysteresis loops for BNT-BKT-100xST ceramics with x = 0.15, 0.20, 0.25, 0.30 at room temperature.

were also obtained under 105kV/cm in $(1-x)(0.75Bi_{0.5}Na_{0.5}TiO_3\text{-}0.25Bi_{0.5}K_{0.5}TiO_3)\text{-}xBiAlO_3$ ternary lead-free AFE ceramics prepared by the two-step sintering method at x=0.06[8]. Recently, Ba, La, Zr co-doped BNT-based lead-free AFE ceramics prepare by conventional sintering technique showed high P_{sat} and high recoverable energy storage density of 37.5 μC/cm^2 and 1.58 J/cm^3, respectively, due to its AFE-like double *P-E* loops with near-zero P_r (Fig. 25)[64].

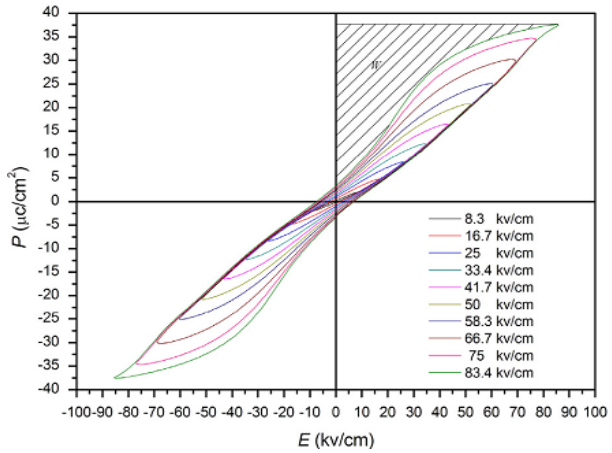

Fig. 25. *P-E* hysteresis loops of $[(Bi_{1/2}Na_{1/2})_{0.94}Ba_{0.06}]La_{(1-x)}Zr_xTiO_3$ ceramics with x=0.02.

In past few years, although great progress has been made in the energy storage properties of BNT-based lead-free AFE ceramics, their energy density was still not satisfactory due to the unstable AFE phase. Recently, $AgNbO_3$ based lead-free ceramics have become a good AFE candidate, showing both high P_r and J_{rec}. Wei *et al*. successfully fabricated dense $AgNbO_3$ ceramics (relative density ~ 97%) using solid state sintering under flowing oxygen, which showed a recoverable energy density as high as high 2.1J/cm^3[65]. However, in their work, because of the weak AFE phase stability of pure $AgNbO_3$ under a low switching electric field at room temperature, the double *P-E* loop character of $AgNbO_3$ was not well developed, leading to a low J_{rec}. In order to obtain higher J_{rec}, a more stable AFE phase with a larger E_A is preferred. Phase stability of a perovskite structure (ABO_3) can be evaluated in terms of tolerance factor *t*, which is defined as[53]

$$t = \frac{(R_A + R_O)}{\sqrt{2}(R_B + R_O)} \tag{10}$$

where R_A, R_B and R_O are the ionic radii of A-site cation, B-site cation and oxygen anion, respectively. Generally, FE phase is stabilized when $t > 1$, while AFE phase is stabilized when $t < 1$. Stable $AgNbO_3$ ceramics can be achieved by replacing the A-site cation Ag^+ with smaller Mn^{4+} ion to decrease the tolerance factor *t*. As a result, J_{rec}, and η were improved from 1.6 J/cm^3 to 2.3 J/cm^3 and from 37% to 57%, respectively, with the doping of 0.1 wt% MnO_2 (Fig. 26)[66]. Besides, a good temperature stability of J_{rec} was obtained in a wide temperature range of 20-180℃. Tian *et al*.

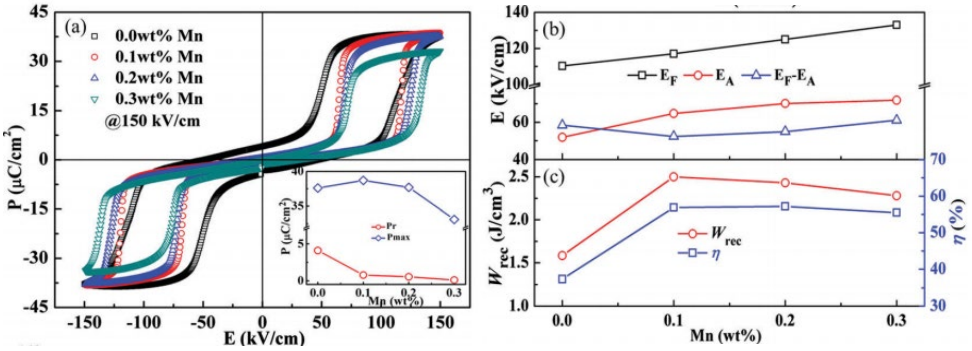

Fig. 26. (a) Hysteresis loops, (b) E_F, E_A, and E_F-E_A, and (c) W_{rec} and η of Mn-doped $AgNbO_3$ ceramic samples at 150 kV/cm. Inset of (a) shows P_r and P_{max}.

doped Bi^{3+} ion, which has a smaller ionic radius (1.17Å) than Ag^{+} (1.28Å), into $AgNO_3$ AFE ceramics to reduce the tolerance factor t[67, 68] and achieve a more stable AFE phase, as presented in Fig. 27. As a result, a high recoverable energy density of 2.6 J/cm^3 and a high energy efficiency of 86% were achieved in $Ag_{0.91}Bi_{0.03}NbO_3$.

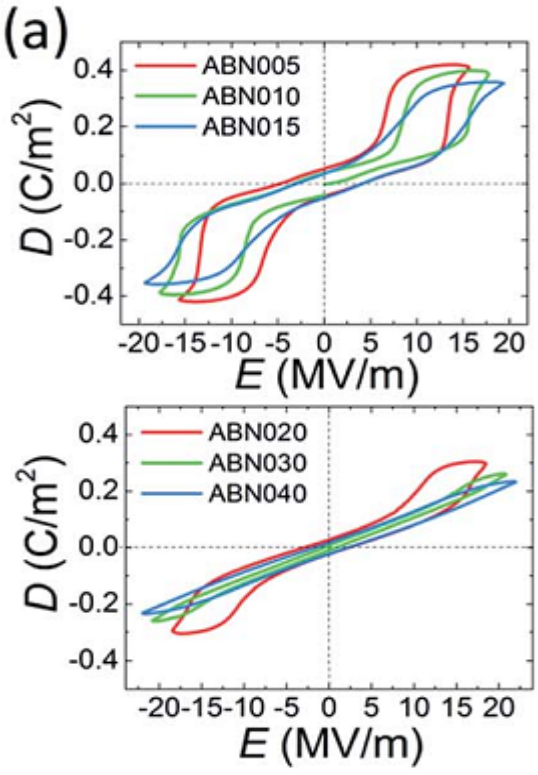

Fig. 27. D-E hysteresis loops of $Ag_{1-3x}Bi_xNbO_3$ ceramics measured at 10 Hz.

Interestingly, Li *et al*. that the stability of $AgNbO_3$ ceramics can be improved (Fig. 28(a)) even by replacing Nb^{5+} with Ta^{5+}, both having the same ionic radius of 0.64Å[68, 69]. The smaller polarizability of Ta^{5+} (2.82Å^3) than that of Nb^{5+} (3.10Å^3) is thought to make the B-site cations less sensitive to the applied electric field, thus leading to high E_F and E_A[70]. Besides, as seen from the Fig. 28(a), with the increase of Ta content, the *P-E* loop became more and more slim, indicating the enhancement of η. As shown in Fig. 28(b), the maximum recoverable energy storage density of 4.2 J/cm^3 was obtained in $Ag(Nb_{0.85}Ta_{0.15})O_3$ ceramic, which is so far the largest value reported in lead-free ceramics.

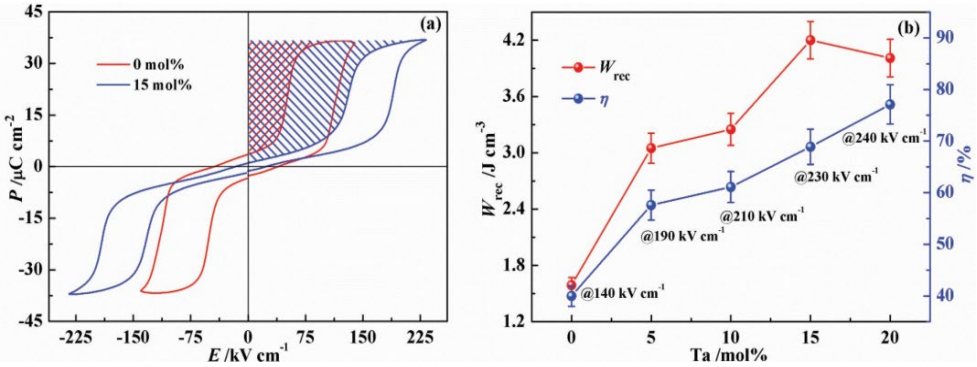

Fig. 28. (a) Hysteresis loops of $AgNbO_3$ and $Ag(Nb_{0.85}Ta_{0.15})O_3$ ceramics. (b) Energy storage performance of $Ag(Nb_{1-x}Ta_x)O_3$ ceramics prior to their breakdown.

3.4. Energy storage in lead-free glass ceramics

As shown in Eq. (7), high BDS is very important for obtaining large J_{rec}. However, because of the existence of many defects, the BDS of the ceramic is usually not too high, which limits the application range of ceramic based capacitors. For

example, pure $Ba_{0.4}Sr_{0.6}TiO_3$ (BST) was not applicable for energy-storage application due to its small energy density of about 0.1 J/cm^3 resulting from the low BDS[71]. The value of the BDS is known to be influenced by factors such as grain size[57], porosity[58], secondary phase[59], interfacial polarization[60], and charge transport[72]. Embedding glass into ceramic matrix can improve the density, reduce the grain size of the ceramics, and decreased the electric field across the grain boundaries, favorable for improving the BDS value. Zhang *et al*. found that by introducing 20 vol% $BaO\text{-}SiO_2\text{-}B_2O_3$ glass into the $Ba_{0.4}Sr_{0.6}TiO_3$ ceramic, the BDS could reach as high as 23.9 kV/mm, which was 1.9 times larger than that of pure $Ba_{0.4}Sr_{0.6}TiO_3$ ceramic (12.1 kV/mm), due to decreased porosity and reduced grain size and pore size, thus resulting in enhanced energy density. The introduction of $Bi_2O_3\text{-}B_2O_3\text{-}ZnO$ glass could also significantly reduce the grain size and improve the density of the $Ba_{0.4}Sr_{0.6}TiO_3$ ceramic, as displayed in Fig. 29, leading to increased BDS. The highest energy storage density of 0.62 J/cm^3 was obtained in ceramics with 5 wt% glass additive[73]. Zhang *et al*. investigated the influence of

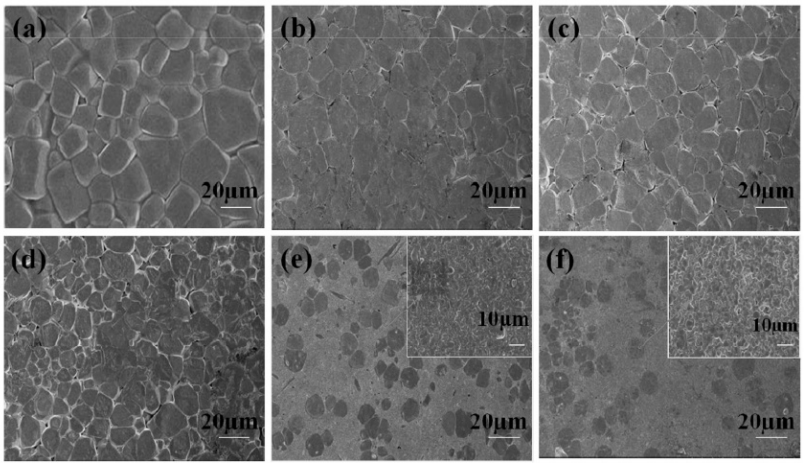

Fig. 29. SEM micrographs of BST ceramics with different glass additives (a) x=0; (b) x=1; (c) x=3; (d) x=5; (e) x=7; (f) x=9.

BaO-SrO-TiO_2-Al_2O_3-SiO_2-BaF_2 glass on the grain size and the BDS of $BaTiO_3$ ceramics in detail and derived a quantitative relation between grain size and BDS, as shown in Fig. 30[72]. Particularly, they found besides the grain size, in the glass-added $BaTiO_3$ ceramics, the BDS was also related to the charge transport across the grain boundary space-charge depletion layer, and was inversely proportional to the average field strength (E_{GB}) in the grain boundary space-charge layer. The E_{GB} could be written as:

$$E_{GB} = E(\frac{d_B}{d_{GB}}) \tag{11}$$

where d_B and d_{GB} denoted the grain size, and the width of the grain boundary space charge layer. With increasing glass content, the grain size is reduced and, consequently, the average applied field in the grain boundary space-charge layer is decreased, and so does the BDS value. Hence, the discharged density is enhanced. These results were also confirmed in B_2O_3-Al_2O_3-SiO_2 doped $Ba_{0.85}Ca_{0.15}Zr_{0.1}Ti_{0.9}O_3$ ceramics[74]. Chen *et al*. studied the

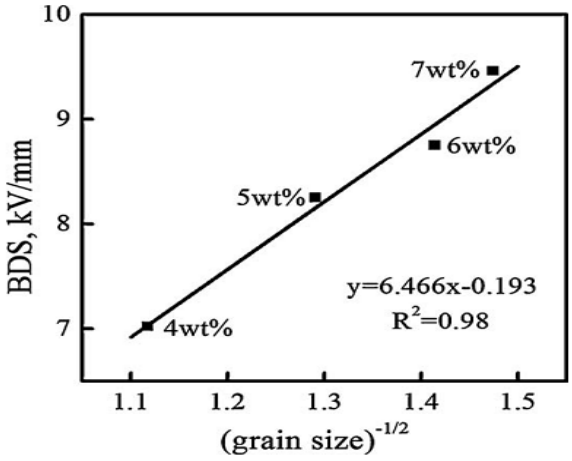

Fig. 30. Dielectric breakdown strength versus (grain size)$^{-1/2}$ for the glass-added $BaTiO_3$ ceramics.

effect of SrO-B_2O_3-SiO_2 (SBS) glass on the BDS of BST ceramics and found that the BDS increases with increasing glass addition and shows an approximate $(\varepsilon_r)^{-1/2}$ dependence, as shown in Fig. 31. A discharge energy density of 0.44 J/cm^3 and an energy efficiency of 67.4%, which were 4 and 3 times more than those of pure BST ceramics, respectively, were obtained in BST ceramic with 2.0 wt% SBS glass addition. A reverse boundary layer capacitor (RBLC) model was recently proposed by Wei *et al*. in the study of glass-doped ceramics, where the glass phase acted

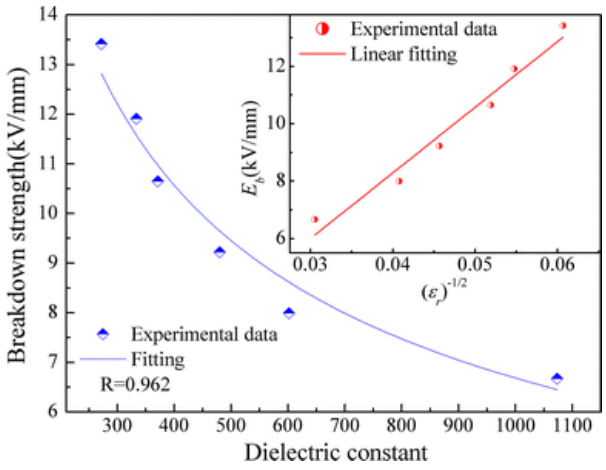

Fig. 31. Breakdown strength as a function of dielectric constant for $Ba_{0.4}Sr_{0.6}TiO_3$ ceramics with different glass additions (The dielectric constant for samples was measured at 1 kHz).

as grain boundaries having an electrical conductivity one or two orders of magnitude higher than that of the ceramic grains. Larger electric field was then dropped on the grains, leading to high BDS[75-76]. In this mode, the electric field values at grain and grain boundary can be calculated by a simple serial model of resistor layers:

$$E_g = \delta_{gb} \frac{(d_g + d_{gb})}{\delta_{gb} d_g + \delta_g d_{gb}} \times E_{avg} \qquad (12)$$

$$E_{g_b} = \delta_g \frac{(d_g + d_{gb})}{\delta_{gb} d_g + \delta_g d_{gb}} \times E_{avg} \quad (13)$$

where E_g, E_{gb} and E_{avg} are the electric field strength corresponding to grain, grain boundary and average value, respective. δ_g and δ_{g_b} are the electric conductivities corresponding to grain and grain boundary, respectively. d_g and d_{g_b} are the thickness values corresponding to grain and grain boundary, respectively. When a high electric field is applied on the ceramic, breakdown may easily occur at the vicinity of pores, electrode edge, and other structural defects.

3.5. Energy storage in lead-free films

As discussed above, the energy storage capacity of lead-free bulk materials is very limited due to their low BDS induced by the many internal defects. Although some advanced sintering techniques, such as spark plasma sintering, liquid phase sintering (glass doping) and discharge plasma sintering, are able to refine the microstructure and reduce the grain size of bulk ceramics, resulting in the improvement of the BDS to some extent, energy storage density of bulk materials is still too low for the practical applications. Compared with bulk materials, thin and thick films have fewer defects and thus possess higher BDS, in favor ofhigh energy density.

Fei *et al*. studied energy storage properties of Mn-doped 0.7($Na_{0.5}Bi_{0.5}$)TiO_3 -0.3$SrTiO_3$ (0.7NBT-0.3ST) relaxor thin films grown on Pt/Ti/SiO_2/Si substrates via a sol-gel method[77] and found that the BDS value and the P_{max}-P_r values of the 0.7NBT-0.3ST thin film were both improved obviously due to Mn doping with

appropriate content. Doped Mn acts as trap site with a deep trap level, leading to improved BDS. Defect dipoles provide intrinsic restoring forces, resulting in the deduction of P_r in Mn-doped films. The compressive stress introduced by Mn^{2+} doping made the Gibbs free energy flat and reduced the ferroelectric domain reversal barrier, thereby increasing the P_{max}. High BDS of 1894 kV/cm and the huge P_{max}-P_r value of 56 μC/cm^2 result in a giant recoverable energy storage density of 27 J/cm^3 in 1 mol. % Mn-doped 0.7NBT-0.3ST thin film. Won *et al*. prepared $BiFeO_3$-doped $(K_{0.5}Na_{0.5})(Mn_{0.005}Nb_{0.995})O_3$ (KNMN) thin films by chemical solution deposition and found that 6 mol% BF-doped KNMN thin films exhibited more slim *P*-*E* hysteresis loops, higher P_{max} and smaller P_r, as shown in Fig. 32. The film can withstand an electric field up to 2 MV/cm and exhibit a recoverable energy density of 28 J/cm^3, with an energy efficiency of 90.3%. In addition, the film capacitors showed a fast discharge time (Fig. 33) and a good temperature stability (Fig. 34)[78]. Jia *et al*. prepared high-quality epitaxial $BaZr_{0.2}Ti_{0.8}O_3$ thin films on Nb-doped $SrTiO_3$ (001) substrates by using radio-frequency magnetron sputtering ,

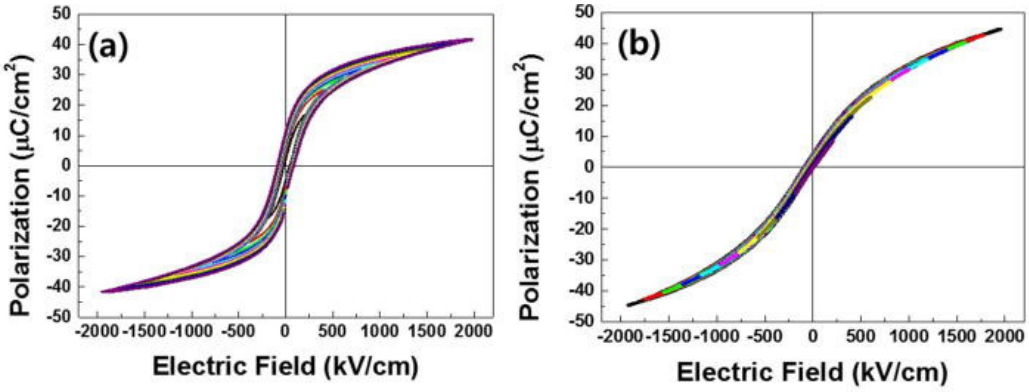

Fig. 32. *P*-*E* hysteresis loops of (a) pure KNMN thin films and (b) 6 mol % BF-doped KNMN thin films. The measurement frequency is 1 kHz.

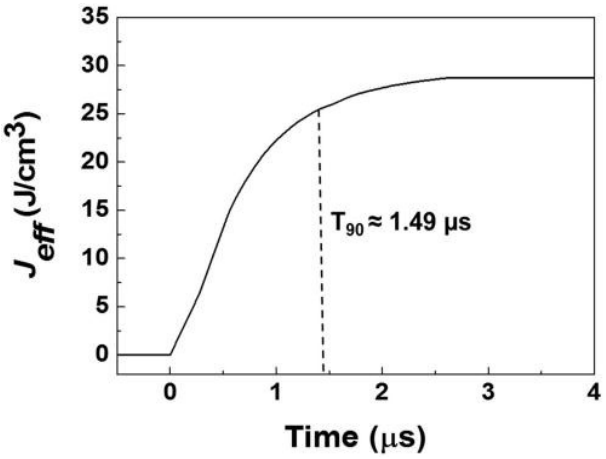

Fig. 33. Effective recoverable energy storage density as a function of discharging time of 6 mol. % BF-doped KNMN thin film capacitors connected to 1 kΩ load resistor (R_L) at the applied electric field of 2 MV/cm. The experimental discharge time t_{90} means the time to reach 90% of the saturated J_{eff} value.[2]

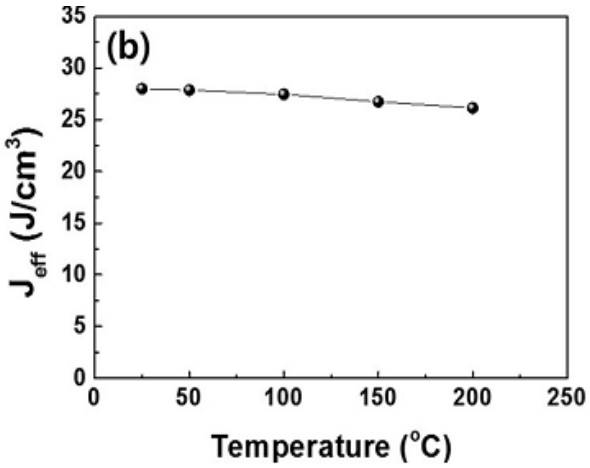

Fig. 34. Effective recoverable energy storage density of 6mol. % BF-doped KNMN thin film capacitors with increasing temperature to 200 ℃. The electric field is 2MV/cm and the charge/discharge frequency is 1 kHz.

which showed a large room-temperature energy storage density of 30.4 J/cm^3 and a high energy efficiency of 81.7% under an electric field of 3 MV/cm (Fig. 35)[79]. Moreover, the BZT film capacitors also exhibited good thermal stability and fatigue

endurance (up to 10^6 cycles) in a wide temperature range from room temperature to 125 °C. Recently, an ultrahigh

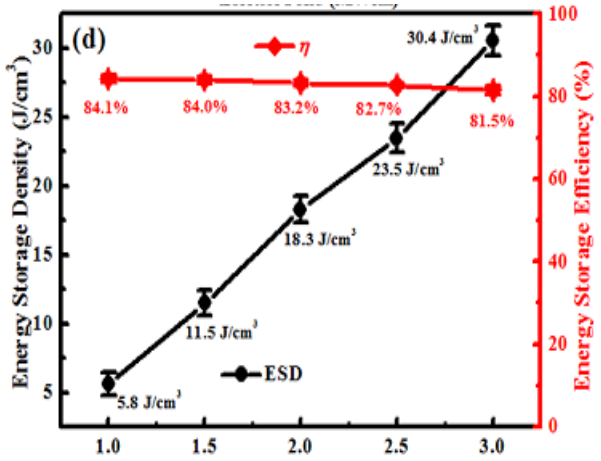

Fig. 35. Energy density and efficiency for BZT thin film depending on electric field

energy density of ~51 J/cm^3 and an efficiency of 64% were obtained in 0.5 mol% Mn-doped 0.4$BiFeO_3$-0.6$SrTiO_3$ relaxor ferroelectric thin film deposited by PLD, at the breakdown strength of 3.6 MV/cm[80]. Simultaneously, the film also exhibited excellent fatigue endurance of 2×10^7 cycles and good thermal stability in a wide temperature range of -40-140℃. These excellent properties were ascribed to the good epitaxial quality, low leakage current and strong relaxor behavior of the film. So far, the largest energy storage density (154 J/cm^3) reported was found in pulsed laser deposited $(Bi_{1/2}Na_{1/2})_{0.9118}La_{0.02}Ba_{0.0582}(Ti_{0.97}Zr_{0.03})O_3$ epitaxial lead-free relaxor thin films at the electric field of 3500 kV/cm, as displayed in Fig. 36[81]. High epitaxial quality, great relaxor dispersion, and the coexistence of FE/AFE phase near the MPB were responsible for the super high energy storage properties of the thin film.

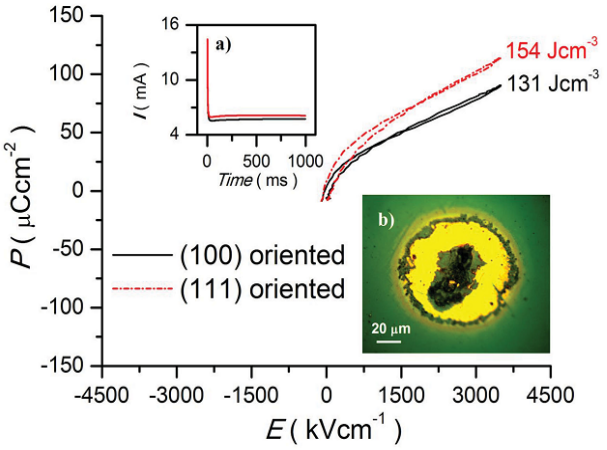

Fig. 36. P-E loops of (100)-and (111)-oriented BNLBTZ thin films at 3500 kV cm^{-1}(close to the breakdown electric field of the thin film) and 10 kHz. The inset (a) is the leakage current at 3500 kV cm^{-1}, and the inset (b) is the optical image of a broken electrode.

Although lead free thin films possess larger energy storage density, their overall stored energy is restricted by their small thickness. Comparatively, thick films (>1μm) could provide sufficient total energy to meet the demands of high energy capacitors[82]. Zhang *et al*. prepared 0-10 wt% $BaO-B_2O_3-SiO_2$ glass doped $(Na_{0.5}Bi_{0.5})TiO_3$ lead-free thick films on alumina substrates via a screen printing method. Unfortunately, the maximum recoverable energy storage density and efficiency were only 2.0 J/cm^3 and 44.1 %, respectively, which are even smaller than some of the ceramics. Recently, by using polyvinylpyrrolidone (PVP)-modified sol-gel technique, Hao *et al*. successfully fabricated dense and void-free lead-free ferroelectric $Na_{0.5}Bi_{0.5}TiO_3$ thick films on $LaNiO_3$/Si (100) substrates[83]. A recoverable energy storage density of 12.4 J/cm^3 and an efficiency of 43% were achieved at 1200 kV/cm. However, compared with thin film, the leakage current density of the NBT thick film was too large and the resulted BDS was too smaller. For NBT film, the leakage

current density strongly depends on oxygen vacancies $V_O^{2-\bullet\bullet}$. In order to improve the BDS, the same group prepared Mn-doped $Na_{0.5}Bi_{0.5}TiO_3$ ferroelectric thick films, where the Ti^{4+} ions were substituted by acceptor Mn^{2+} ions and the defects of $(Mn_{Ti^{4+}}^{2+})''$ were formed meanwhile, which could restrict the movement of $V_O^{2-\bullet\bullet}$, and thus decreased the leakage current. When the Mn content was 1 mol%, the thick film exhibited the highest BDS value and the largest value of P_{max}-P_r because of the smallest leakage current density (Fig. 37). As a result, superior energy storage density of 30.2 J/cm^3 and energy efficiency of 47.7% at 2310 kV/cm were achieved[84].

Besides pure BNT, energy storage properties of BNT-based solid solution thick films have also been studied. An *et al*. fabricated (1-*x*%)NBT- *x*%$SrTiO_3$ (*x*=0, 0.05, 0.10, and 0.15) thick films on $LaNiO_3$/Si(100) substrates using a PVP modified chemical solution route. They found that with the introduction of ST, the BDS and P_{max}-P_r increased. Among all the thick films, the sample with *x*=0.05 showed the highest recoverable energy density of 36.1 J/cm^3. Besides, the energy storage was stable in the temperature range from room temperature to 80℃ and a low leakage current density of 1.93×10^{-5} was achieved[85].

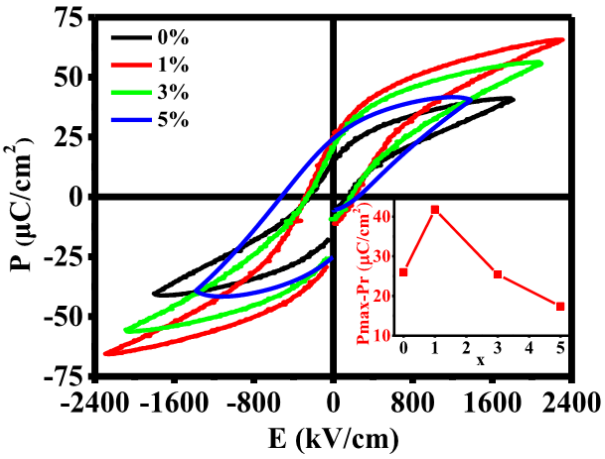

Fig. 37. *P-E* loops of NBTMnx thick films measured at their BDSs and at room temperature. The inset shows the corresponding P_{max}-P_r values.

3.6. Energy-storage in lead-free polymer-based nanocomposites

Ferroelectric polymers, such as PVDF, P(VDF-TrFE), and P(VDF-HFP), which possesses high BDS, low dielectric loss, and good machinability, are superior candidates for dielectric capacitors. However, due to small P_{sat}, energy storage densities of these polymers are low and even smaller than some of the ceramics[86]. For instance, the current best commercial biaxial oriented polypropylenes (BOPP) possess rather low energy density (3 J/cm^3 at the electric field of 5000 kV/cm), which seriously limits their applications[86]. In order to solve these problems, ceramic-polymer based nanocomposites are proposed as they combine high P_{sat} of the ceramic fillers with large BDS value of the polymer matrix.

Due to poor interfacial compatibility between inorganic filler and organic matrix, the energy storage capacity of the nanocomposites filled with untreated fillers is limited. To mitigate the poor interfacial compatibility, and the agglomeration and inhomogeneity of the fillers in polymer matrix, surface modification of the ceramic fillers is indispensable. For instance, surface modified $BaTiO_3$ particles displayed better dispersion within the polymer matrix, resulting in enhanced BDS value and reduced dielectric loss[87]. Gao *et al*. proposed a novel way to improve the interface of BT/PVDF nanocomposites[88], that is, the surface of BT was hydroxylated by H_2O_2, followed by modifying with a titanate coupling agent DN-101. Compared with

PVDF/DN-101-$BaTiO_3$(D-BT) nanocomposites, PVDF/H_2O_2-DN-101-$BaTiO_3$ (D-h-BT) nanocomposites showed larger saturated polarization and BDS. The charge energy density increased from 6.5 to 9.01 J/cm^3, and the discharge energy density improved from 3.01 to 4.31 J/cm^3, as shown in Fig. 38. Besides, core-shell structure

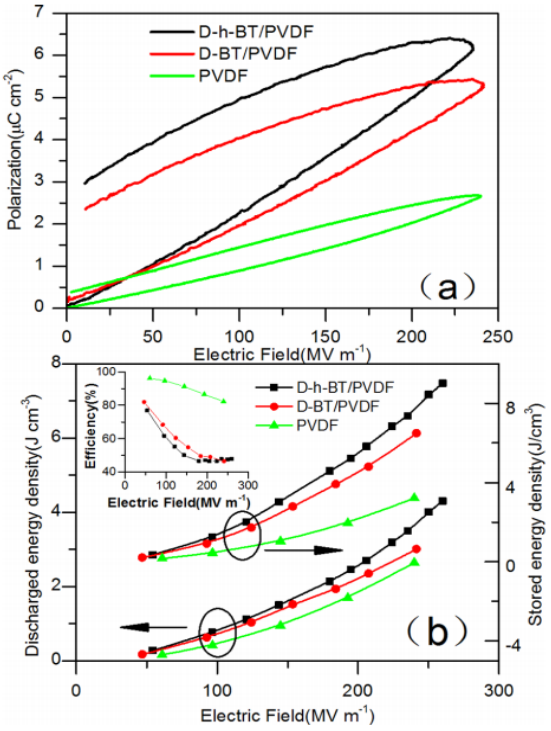

Fig. 38. (a) Polarization and (b) energy density of PVDF film, D-BT/PVDF, and D-h-BT/PVDF nanocomposite films.

has been demonstrated to be beneficial to the improvement in the dispersion of nanoparticles in polymer matrix. Su *et al*. successfully prepared $BaTiO_3$@sheet-like TiO_2 core-shell nanoparticles (NPs) and made them well-dispersed into PVDF[89]. The PVDF films with 2.5 vol% BT@TiO_2 NPs exhibited higher electric displacement (6.0 μC/cm^2) than that of PVDF films with 2.5 vol % BT NPs (5.1 μC/cm^2) under the same electric field of 350 kV/mm, which was resulted from the interfacial polarization induced by the large surface area of TiO_2 nanosheets assembled on BT NPs in the

nanocomposites (Fig. 39). At the same time, as the buffer layer between the BT NPs and polymer matrix, TiO_2 smoothed the inhomogeneous electric field in the nanocomposites, resulting in the enhancement of BDS (490 kV/mm with 2.5 vol % BT@TiO_2 NPs) compared with that of the pristine PVDF. Finally, a high energy density of 17.6 J/cm^3 was obtained in the nanocomposites with 2.5 vol % BT@TiO_2 NPs due to enhanced electric displacement and BDS value. Jiang *et al*. developed a

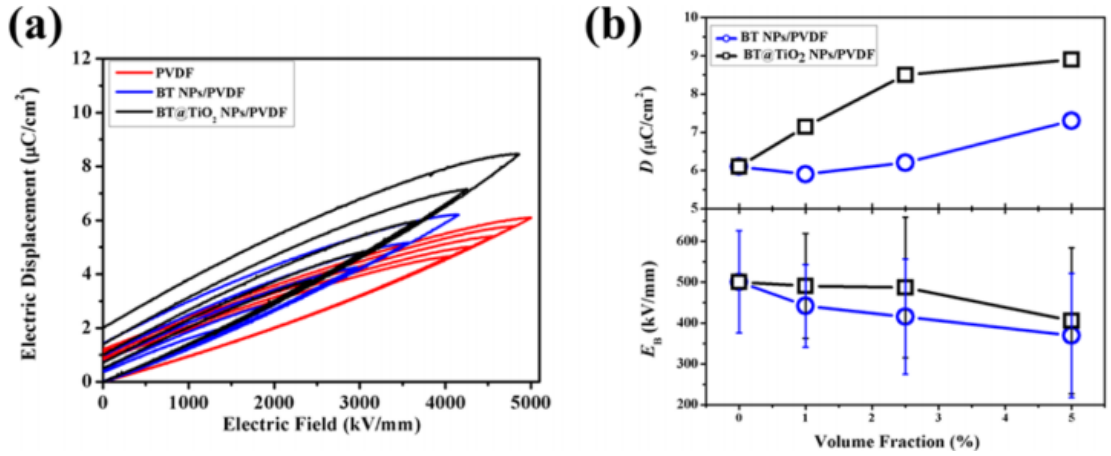

Fig. 39. (a) Unipolar electric displacement-electric field loops of composites films of BT and BT@TiO_2 NPs with different volume fraction of 2.5%. (b) Variation of maximum electric displacement and characteristic breakdown strength with different volume fraction of nanofillers for PVDF nanocomposites embedded with BT and BT@TiO_2 NPs.

core@double-shell structure to prepare barium titanate (BT)-based polymer nanocomposites with high energy storage density[90]. As displayed in Fig. 40, the core is BT nanoparticles possessing high dielectric constant while the first shell is hyperbranched aromatic polyamide (HBP) and the second shell is poly(methyl methacrylate) (PMMA) grafted from the terminal groups of HBP via atom transfer radical polymerization. The electric displacement and energy density increased

significantly with increasing loading of BT nanoparticles, as seen in Fig. 41.

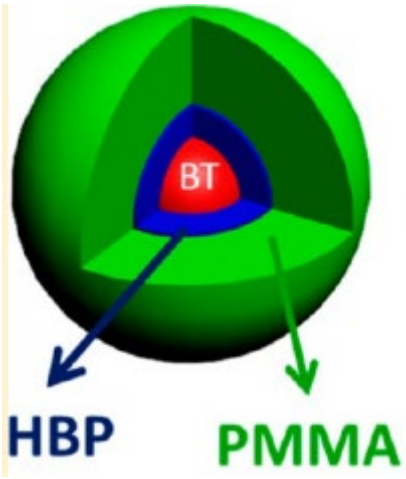

Fig. 40. The double-shell structure of BT@HBP@PMMA nanocomposites.

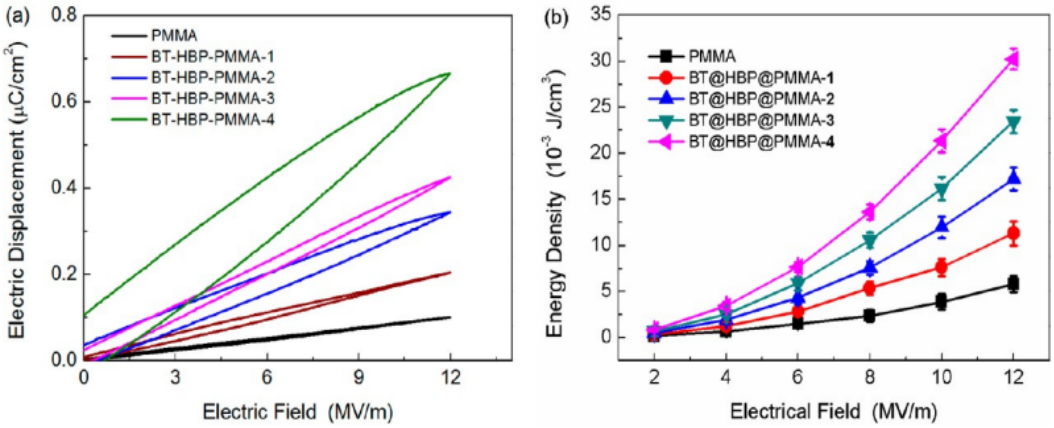

Fig. 41. (a) Electric displacement-electric field (D-E) loops of the PMMA and BT@HBP@PMMA nanocomposites. (b) Energy density of the PMMA and BT@HBP@PMMA nanocomposites under different electric field. The BT contents in BT@HBP@PMMA-1, BT@HBP@PMMA-2, BT@HBP@PMMA-3, and BT@ HBP@PMMA-4 represents are 25.5, 41.4, 51.7, and 56.7 vol %, respectively.

Compared with spherical nanoparticles, nanofibers, nanowires, nanotubes, and nanorods etc. with large aspect-ratio can increase the polarization of nanocomposites at much lower concentrations because their large dipole moments, and their smaller

specific surface can help to reduce the surface energy and thus prevent the nanofillers from agglomerating in the polymer matrix. For example, a small content of dopamine-modified $Ba_{0.6}Sr_{0.4}TiO_3$ nanofibers (BST NFs)-filled PVDF nanocomposites displayed more than doubled energy density as compared with pure PVDF matrix due to the combined effect of surface modification by dopamine and large aspect ratio of the BST nanofibers (Fig. 42)[91]. Zhai *et al*. prepared a small

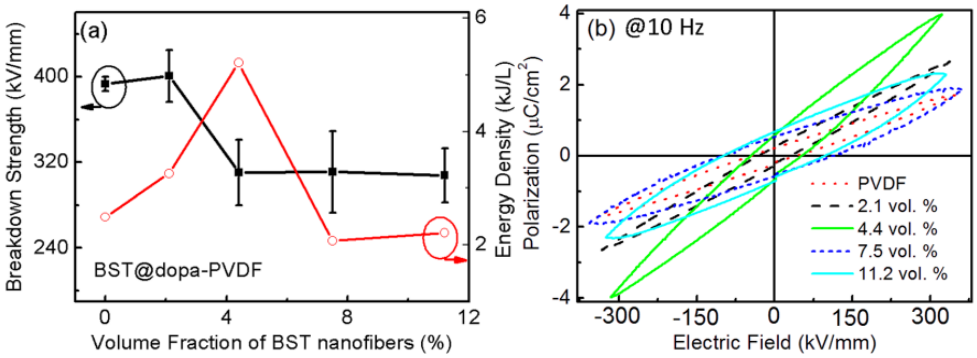

Fig. 42. (a) Variations of the breakdown strength and energy density of the BST/PVDF composite films with the volume fraction of dopamine-modified BST nanofibers, and (b) room temperature *P-E* loops of PVDF-based composites filled with different volume fractions of dopamine-modified BST nanofibers.

loading of 3-aminopropyltriethoxysilane (APS)-modified $Ba_{0.6}Sr_{0.4}TiO_3$ nanofiber-filled PVDF nanocomposites. The maximum energy density of ~6.8 J/cm^3 at 3800 kV/cm, which was about 143% higher than that of the PVDF (~ 2.8 J/cm^3 at 4000 kV/cm), was obtained in the nanocomposite with 2.5 vol% APS-modified BST NFs. The superior energy storage properties were ascribed to the combined effects of surface modification by the APS, and large aspect ratio of BST NFs[92]. Similarly, the PVDF-based composites containing 2.5 vol% PVP modified $SrTiO_3$ NFs exhibited an energy storage density of 6.8 J/cm^3 at 3800 kV/cm[93]. Moreover, the efficiency of the

composites is higher than 85% at electric fields below 1000 kV/cm and is still higher than 60% at an electric field of 3800 kV/cm, as shown in Fig. 43. The BDS value of PVP modified ST NF/PVDF was found to be higher than that of untreated ST NF/PVDF (Fig. 44) and slightly lower than that of pure PVDF which demonstrated that PVP-modified ST NFs dispersed well in the PVDF matrix (Fig. 45).

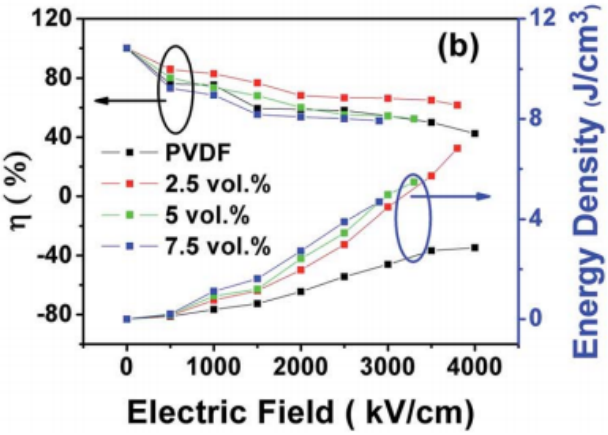

Fig. 43. (a) D-E loops of nanocomposites filled with different volume fractions of PVP modified ST NFs at 100 Hz and room temperature. (b) Energy storage density and efficiency of nanocomposites.

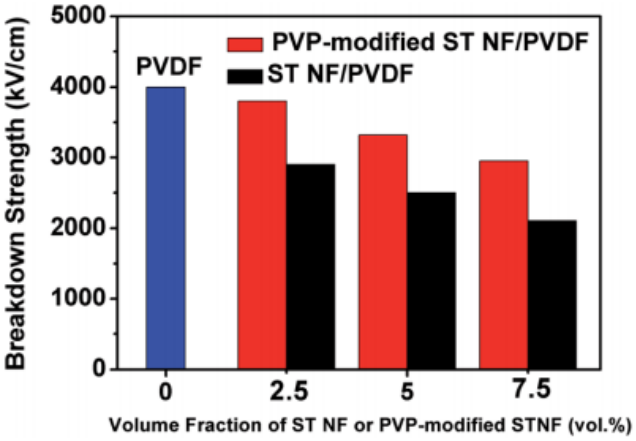

Fig.44. Breakdown strength of nanocomposites with different amounts of untreated ST NFs and modified ST NFs.

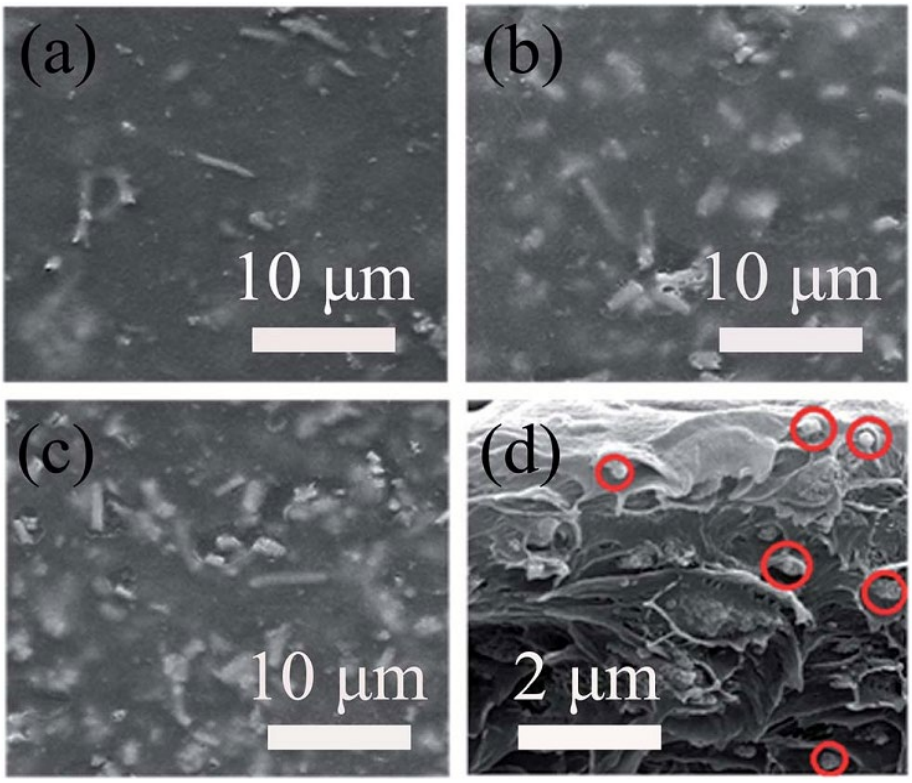

Fig. 45. The surface SEM images of nanocomposites filled with (a) 2.5 vol%, (b) 5 vol%, and (c) 7.5 vol% of modified ST NFs. (d) Cross-section SEM of nanocomposites filled with 5 vol% of modified ST NFs.

A high discharge energy density of 14.86 J/cm^3 at 450 MV/m was achieved in PVDF-based nanocomposites with BST nanowire fillers[94]. The high BDS value and enhanced P_{sat} induced by the incorporation of BST nanowires contributed to the large energy density. An energy density of 7.03 J/cm^3 was obtained in PVDF based nanocomposites with a small amount of dopamine coated $BaTiO_3$ nanotube fillers at a relatively low field of 330 MV/m by Zhai *et al*[95]. Recently, they also fabricated a novel inorganic/polymer nanocomposite, using 1-dimensional TiO_2 nanorod arrays as fillers and PVDF as matrix and studied the effect of the height ratio of TiO_2 on the energy storage properties of nanocomposites[96]. This new structure exhibited a large enhancement in the electric polarization, leading to a significant improvement on the

energy density and efficiency. The maximum discharge energy density of 10.62 J/cm^3 and an efficiency of about 70% at the applied electric field of 340 MV/m were achieved in the nanocomposites with TiO_2 nanorod array fillers of 18% height ratio.

Nowadays, it has already been confirmed that the interfacial polarization is the main polarization mechanism in polymer nanocomposites[97-98]. However, as the ceramic nanofiller content increases, considerable agglomerations and many defects such as voids are introduced into the nanocomposites, leading to a sharp decrease in the breakdown strength. Therefore, in nanocomposites, it is hard to obtain high P_{sat} and large BDS simultaneously. To solve this problem, Nan *et al*. used core-shell structured $BaTiO_3$@TiO_2 nanofibers as fillers in PVDF matrix and found that the electric displacement was increased significantly due to the additional polarization induced in the interfacial zone by the charge shifting between the BTO core and the TO_2 shell. High BDS was maintained because the charge shifting was limited to the interfacial zone and a charge percolation path cannot be formed in the matrix, as shown in Fig. 46[99]. As a result, both high polarization and large BDS were obtained. A large discharge energy density of about 20 J/cm^3 was achieved at the electric field of 646 kV/mm, which was higher than the BDS of pure PVDF (599 kV/mm), in the nanocomposite filled with only 3 vol% of $BaTiO_3$@TiO_2-NFs. Even at this ultrahigh electric field, the nanocomposite still exhibited an energy storage efficiency of $\approx$ 75%. Similar experiment results were also confirmed by Hu *et al*[100]. Furthermore, by using P(VDF-HFP) as polymer matrix, Nan *et al*. obtained a giant discharge energy density of about 31.2 J/cm^3 at 797.7 kV/mm and a high efficiency of ≈78% in 3 vol%

of BTO@TO-nfs filled nanocomposites (Fig. 47), which were resulted from the substantially enhanced interfacial polarization at the hierarchical interfaces inside the BTO@TO-nfs and the improved BDS value[101]. Apart from the TiO_2 shell, Al_2O_3 shell has also been studied.

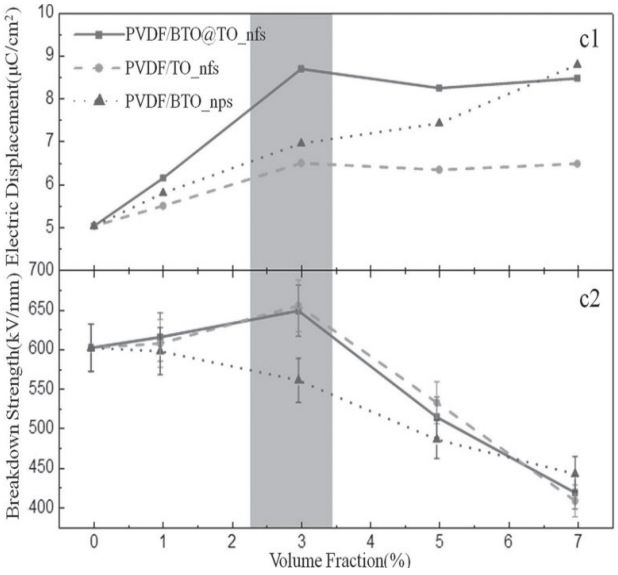

Fig. 46. Variation of (a) maximum electric displacement and (b) breakdown strength with volume fraction of nanofillers (BTO@TO-nfs, TO-nfs and BTO-nps) in PVDF nanocomposites.

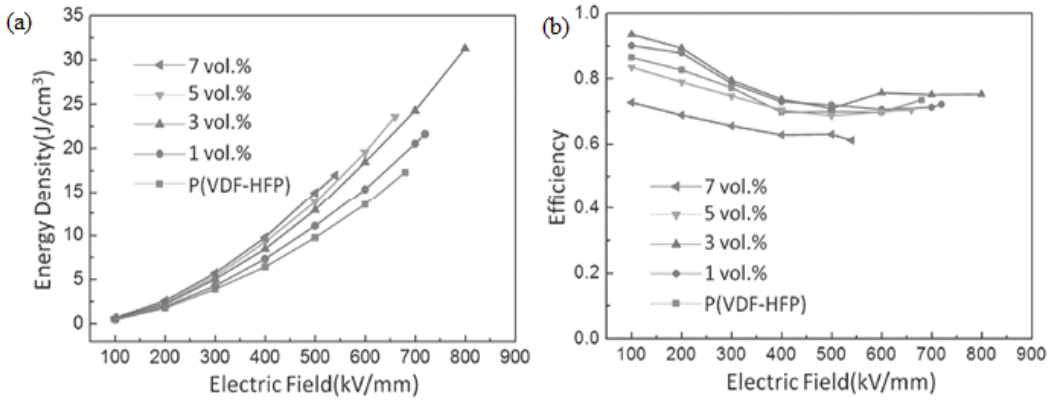

Fig. 47. a) discharge energy density and b) charge-discharge efficiency with electric field for the P(VDF-HFP)/BTO@TO-nfs nanocomposites with different volume fractions of BTO@TO-nfs.

In PVDF-based nanocomposites filled with core-shell structured $BaTiO_3$@Al_2O_3 nanofibers (BT@Al_2O_3 nfs), the moderate interfacial area between the insulating Al_2O_3 shell and BT nfs was found to increase the BDS value and hence the discharge energy density. Besides, the energy loss was reduced because the insulating Al_2O_3 shell blocks the movement of charge carriers. Finally, a high discharge energy density of 12.18 J/cm^3 at 400 MV/m was obtained in the nanocomposite films added with 5 vol% BT@Al_2O_3 nfs[102].

Recently, sandwich-structured nanocomposites embedded with a high-BDS layer have been shown to achieve concurrent enhancement in electric displacement and BDS[103-105]. For example, a sandwich-structured nanocomposite composed of a pure P(VDF-HFP) central layer and two $BaTiO_3$-P(VDF-HFP) neighboring layers was developed by Luo *et al*., as shown in Fig. 48[106]. Compared with the single layer composite, the BDS value and the effective electric displacement (P_{max}-P_r) of the composites with sandwich structure were both improved, as shown in Fig. 49. Hence, the discharge energy density was increased from 2.32 to 5.22 J/cm^3. Similarly, Wang *et al*.

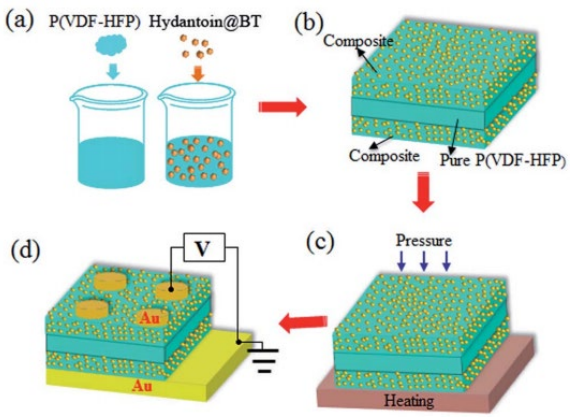

Fig. 48. Diagram for (a) preparing P(VDF-HFP) solution and P(VDF-HFP)

suspension with dispersed hydantoin@BT nanoparticles, (b) preparing the sandwich-structured composite, (c) the process of hot-pressing, (d) sputtering electrode for electrical properties testing. V represents a testing equipment.

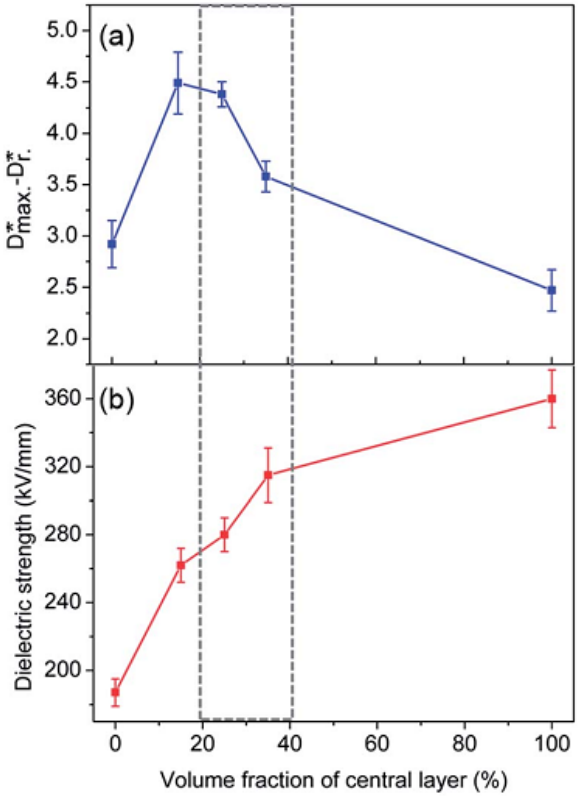

Fig. 49. (a) Effective electric displacement and (b) breakdown strength of the composites as a function of the volume fraction of the central layers.

fabricated sandwich-structured ceramic/polymer nanocomposites with one PVDF middle layer and two barium titanate (BT)/PVDF nanocomposite outer layers[107]. It was found that the content of the BT fillers could change the electric field distribution and thus influence the BDS, energy density and efficiency. At an optimized BT volume fraction of 3 vol%, a discharge energy density of 16.2 J/cm^3 and an efficiency of 70% at the electric field of 410 MV/m were obtained, which were higher than those of pure PVDF. $NaNbO_3$ nanoplatelets were used in a sandwiched composite with two

outer layers of two-dimensional $NaNbO_3$ platelets dispersed in PVDF matrix to provide high electric displacement and one middle layer of pristine PVDF to offer high BDS[108]. By tailoring the content of the $NaNbO_3$ platelets, the BDS value and energy density of the tri-layered composites were improved significantly. The highest discharge energy density of 13.5 J/cm^3 at 400 MV/m was obtained in the trilayer film with 5 vol% $NaNbO_3$.

In above work, the function of middle layer (high-BDS layer) is to block leakage current and improve the BDS value so that the outer layers can be polarized at a higher electric field, enhancing the electric displacement. However, the acquisition of high energy density requires large electric field, which reduce the reliability and limits the application of dielectric capacitors. In order obtain high energy density at a low electric field, Shen *et al*. designed an opposite structure, where a high-ε_r layer was introduced in the central, sandwiched between two high-BDS outer layers, as shown in Fig. 50[109]. By confining the BTO@TO-nfs with high-ε_r layer as the central layer, the electric-field inside the composite will be redistributed with the outer polymer layers (with lower ε_r) polarized at a much higher electric field and the middle layer experienced a lower field, leading to less chance of dielectric breakdown. Hence, the overall BDS of the multilayer nanocomposites will be enhanced. Fig. 51 showed the *P-E* loops of nanocomposites with different structures. Under the same electric field, TSM-02 nanocomposites exhibited the largest P_{max} with an ultrahigh discharge energy density of 12.5 J/cm^3 at a low electric field of 350 kV/mm. At the same time, the TSM-02 nanocomposites delivered high efficiencies of about 80% at 100 kV/mm and

about 60% at 345 kV/mm. Very recently, the same group also investigated the breakdown behavior of polymer nanocomposites under electrostatic stimuli by a comprehensive phase-field model. Based on the high-throughput calculation, they designed a sandwich microstructure for PVDF-$BaTiO_3$ nanocomposite, where the upper and lower layers were filled with parallel nanosheets and the middle layer was filled with vertical nanofibers. The energy density of the PVDF-$BaTiO_3$ nanocomposite with the data-driven designed optimal microstructure could be as high as 2.44 times that of the pure PVDF polymer[110]. Sandwich-structured nanocomposites which were composed of boron

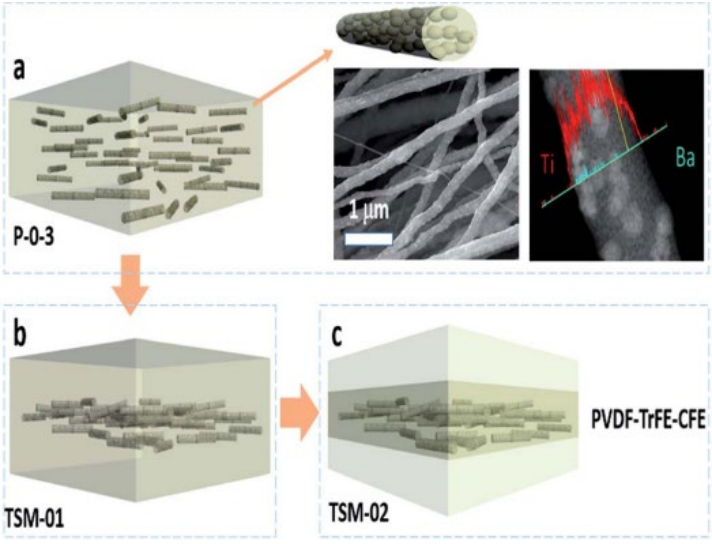

Fig.50. Schematics of the structure of (a) P-0-3 nanocomposites with BTO@TO-nfs randomly dispersed in the PVDF matrix, (b) TSM-01 nanocomposites with BTO@TO-nfs confined within the central layer and (c) TSM-02 nanocomposites with PVDF in the central layer replaced by PVDF-TrFE-CFE. The morphology of the BTO@TO-nfs could be better

distinguished with the SEM and TEM images shown in the inset. The element mapping image reveals the homogeneous dispersion of $BaTiO_3$ nanoparticles inside BTO@TO-nfs.

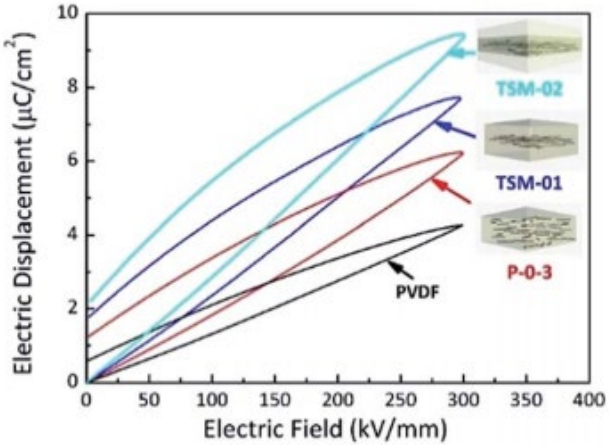

Fig. 51. Electric polarization-electric field (*P-E*) loops of pure PVDF (in black), P-0-3 (in red), TSM-01 (in blue) and TSM-02 (in pale blue) nanocomposites.

nitride nanosheets dispersed in PVDF matrix as outer layers and PVDF with barium strontium titanate (BST) nanowire (NW) fillers as the central layer were also synthesized[111]. The highly insulating outer layers could provide high BDS, while the central layer could offer high ε_r and electric displacement. The energy storage properties of the newly designed trilayer polymer nanocomposite depend on the content of BST NWs. The nanocomposite with 8 vol% BST NWs exhibited the highest breakdown strength, and the electrical displacement was increased greatly with increasing BST content from 6 to 8 vol% and then it nearly kept constant. The resulted highest discharge energy density of 20.5 J/cm^3 was obtained in the nanocomposite with 8 vol% BST NWs. Besides, the discharge time of the trilayer nanocomposite was only 2.22 μs, faster than that of BOPP (2.9 μs), and the energy density was almost unchanged after 50000 charge/discharge cycles (Fig. 52).

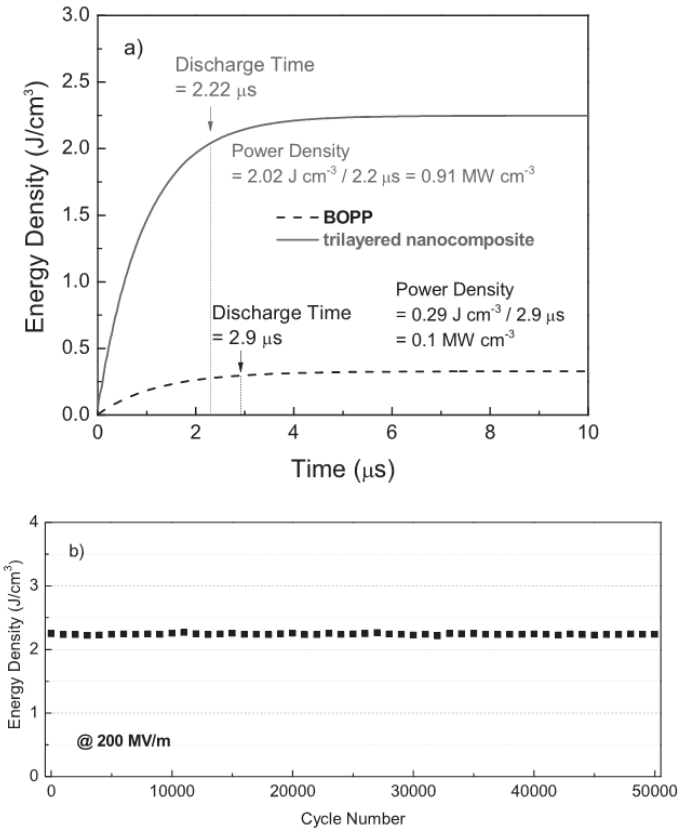

Fig. 52. (a) Discharge energy density as a function of time of BOPP and the trilayer nanocomposites with 8 vol% BST NWs. Both samples are charged under an electric field of 200MV/m. (b) Cyclic stability of the trilayer nanocomposites with 8 vol% BST NWs under 200MV/m.

4. Summary and Future Prospects

In summary, huge progress have been achieved in environmental friendly lead-free dielectric materials (mainly including relaxor ferroelectric/ antiferroelectric ceramics, glass doped ceramics, thin/thick film, and polymer based composites) for energy storage applications. The energy storage properties of some of the lead-free materials are comparable with those of lead-based dielectric materials. However, there are still many problems need to be solved if lead-free dielectric capacitors want to

find a place in emerging applications (such as hybrid electric vehicles, high frequency inverters, insulated gate bipolar transistor (IGBT) snubbers and electrical weapon systems), which require that the capacitors have not only large overall energy, and high recoverable energy and power densities, but also high energy efficiency. To obtain high recoverable energy density and high efficiency, one needs large difference between the saturated polarization and the remnant polarization, high BDS, and slim *P-E* loop, which cannot be simultaneously realized in any of the existing lead-free materials. Table 3 summaries the parameters of some important lead-free dielectric materials for energy storage applications. As seen from Table. 3, ferroelectric ceramics possess low

Tabe 3. The parameters of important dielectric materials for energy storage.

Materials	State	Breakdown Strength (kV/cm)	Dielectric constant	Dielectric loss	Recoverable energy density (J/cm^3)	Energy efficiency	Ref.
$Ba_{0.7}Ca_{0.3}TiO_3$	Bulk ceramic	150	-	-	1.41	61.00%	[14]
$Ba_{0.3}Sr_{0.7}TiO_3$	Bulk ceramic	140	-	0.022	0.57	69.30%	[22]
$Ba_{0.3}Sr_{0.7}TiO_3$	Bulk ceramic(SPS sintering)	230	-	0.0025	1.13	86.80%	[22]
$Ba_{0.4}Sr_{0.6}TiO_3$	Bulk ceramic (Sintered in O_2)	167.2	-	＜0.02	1.081	73.78%	[23]
$0.9BaTiO_3$-$0.1Bi(Mg_{2/3}Nb_{1/3})O_3$	Relaxor bulk ceramic	287.7	4068	0.028	1.13	95.70%	[35]
$0.9K_{0.5}Na_{0.5}NbO_3$-$0.1Bi(Mg_{2/3}Nb_{1/3})O_3$	Relaxor bulk ceramic	300	-	-	4.08	62.70%	[49]
$0.94(0.75Bi_{0.5}Na_{0.5}TiO_3$-$0.25Bi_{0.5}K_{0.5}TiO_3)$-$0.06BiAlO_3$	AFE bulk ceramic	-	-	-	1.15	73.20%	[8]
$[(Bi_{1/2}Na_{1/2})_{0.94}Ba_{0.06}]La_{0.98}Zr_{0.02}TiO_3$	AFE bulk ceramic	-	-	-	1.58	-	[64]
$Ag_{0.91}Bi_{0.03}NbO_3$	AFE bulk ceramic	-	-	-	2.6	86.00%	[67]

$Ag(Nb_{0.85}Ta_{0.15})O_3$	AFE bulk ceramic	233	-	-	4.2	69.00%	[69]
$BaO-B_2O_3-SiO_2-Na_2CO_3-K_2CO_3$ glass doped $Ba_{0.4}Sr_{0.6}TiO_3$ ceramics	Glass-ceramic	280.5	-	-	0.72	-	[75]
$(Bi_{1/2}Na_{1/2})_{0.9118}La_{0.02}Ba_{0.0582}(Ti_{0.97}Zr_{0.03})O_3$	Epitaxial thin film	-	-	-	154	97.00%	[81]
$0.95(Na_{0.5}Bi_{0.5})TiO_3-0.05SrTiO_3$	Thick film	1965	964		36.1	40.80%	[85]
10 vol% H_2O_2-DN-101-$BaTiO_3$ /PVDF	Nano-composites	2600	-	-	4.31	47.83%	[88]
7.5% $Ba_{0.2}Sr_{0.8}TiO_3$ NWs/PVDF	Nano- composites	-	~17.5	-	14.86	-	[94]
2.1 vol % BT-DA NTs/PVDF	Nano-composites	3404	>10	-	7.03	-	[95]
TiO_2 nanorod arrays/ PVDF	Nano-composites	3400	32	＜0.02	10.62	~70%	[96]
3vol%BTO@TO-NFs-P(VDF-HFP)	Nano-composites	7977	-	-	31.2	~78%	[101]
3vol%$BaTiO_3$NPs-PVDF/PVDF/ 3vol%$BaTiO_3$ NPs-PVDF	Sandwich structure	4100	-	-	16.2	70%	[107]
Boron nitride nanosheets-PVDF /BST NWs-PVDF/Boron nitride nanosheets-PVDF	Sandwich structure	5800	14.2	＜0.05	20.5	-	[111]

recoverable energy density and low energy efficiency because of their large P_r and small BDS. Relaxor ferroelectric and antiferroelectric ceramics though exhibit large energy efficiency, their recoverable energy densities are not high enough for practical applications. Thin films have high energy efficiency and large recoverable energy density, but their overall energy is low because of the small volume of the thin films. Thick films and polymer-based composites show high recoverable densities, while their energy efficiencies are too low. Thus, in order to obtain lead-free materials with superior energy storage properties, one can either enhance the BDSs of relaxor ferroelectric and antiferroelectric ceramics or increase the energy efficiencies of thick

films and polymer-based composites.

The BDS of the bulk ceramic is closely related to its microstructure (such as grain size and bulk density), which can be refined by ceramic powder processing techniques, such as sol-gel and co-precipitation for powder preparation and SPS, microwave sintering, and two-step sintering for powder sintering. For antiferroelectric ceramics with “square” hysteresis loops, it’s hard for them to withstand over several hundred of charge-discharge cycles because they are often cracked due to the frequent phase transition during repeated charge-discharge processes. Further efforts should be made to realize more slanted hysteresis loops which are thought to be helpful for increased number of charge-discharge cycles, important for practical applications[112]. Owing to their high P_{sat}, η, and small P_r, antiferroelectrics are anticipated to replace ferroelectrics in the development of high efficiency thick film or composite based capacitors. The principle diagram of high energy density and high efficiency obtained in antiferroelectric-polymer composite capacitors is shown in Fig. 53. Nowadays, polymer based nanocomposites indeed exhibit high room-temperature discharge energy density and high efficiency and they have already been used in high pulse power systems. However, not only in some harsh conditions, such as hybrid electric vehicles, but also in gentle conditions, such as embedded capacitors, power dissipation can increase the operating temperature to 100℃ or higher. A cooling system is thus required for many polymers capacitors, which adds extra energy consumption. More efforts should be made in the future to develop polymer-based capacitor with good thermal stability even at higher temperatures.

As discussed above, until now, the discharge speed, and fatigue character of lead-free dielectric materials for energy storage have rarely been reported, which are critical for obtaining energy storage devices with high power density and long cycle-lives. In the future, more attention should be paid to those factors.

Overall, It is expected that this review will provide some guidance in the development of lead-free capacitors with large recoverable energy density, high power density, high efficiency, and long cycle life.

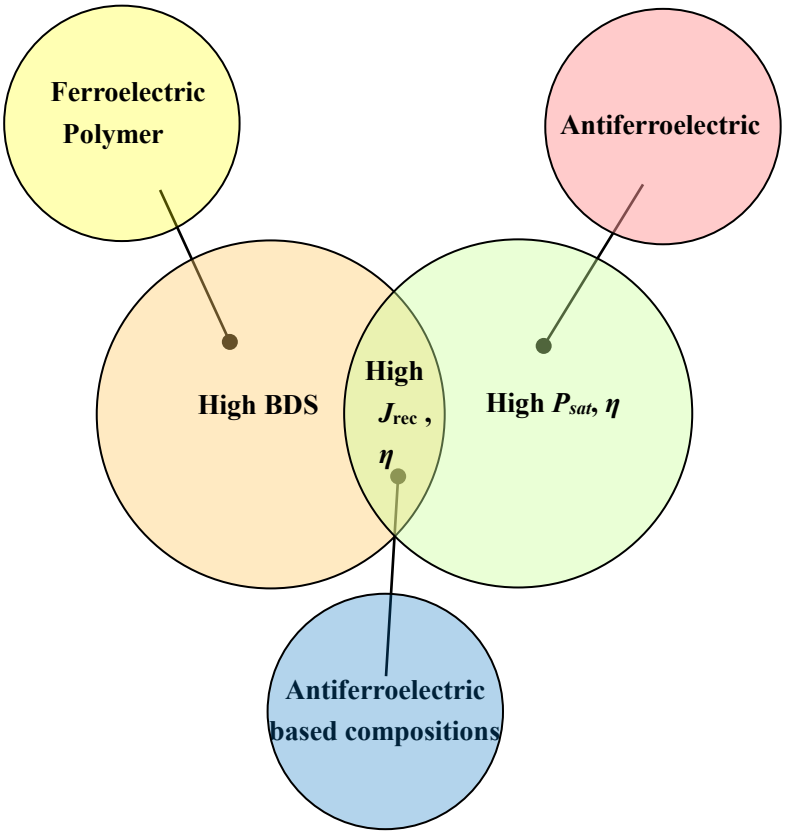

Fig. 53. The principle diagram of high energy density and efficiency obtained in antiferroelectric-polymer composites capacitors

Acknowledgement:
This work was supported by the Research Grants Council of the Hong Kong Special Administrative Region, China (Project No. PolyU152665/16E)

[1] Z. M. Dang, J. K. Yuan, S. H. Yao, R. J. Liao, Flexible nanodielectric materials with high permittivity for power energy storage, Adv. Mater. 25, 6334 (2013).

[2] A. Chauhan, S. Patel, R. Vaish, C. R. Bowen, Anti-Ferroelectric Ceramics for

High Energy Density Capacitors, Materials. 8, 8009 (2015).

[3] K Yao, S Chen, M Rahimabady, MS Mirshekarloo, Nonlinear Dielectric Thin Films for High-Power Electric Storage With Energy Density Comparable With Electrochemical Supercapacitors, IEEE Trans Ultrason Ferroelectr Freq Control. 58, 1968 (2011).

[4] Qi Li, Kuo Han, Matthew Robert Gadinski, Guangzu Zhang, Qing Wang, High Energy and Power Density Capacitors from Solution-Processed Ternary Ferroelectric Polymer Nanocomposites, Adv. Mater. 26, 6244 (2014).

[5] Xihong Hao, Ying Wang, Jichun Yang, Shengli An, Jinbao Xu, High energy-storage performance in $Pb_{0.9}1La_{0.09}(Ti_{0.65}Zr_{0.35})O_3$ relaxor ferroelectric thin films, J. Appl. Phys. 112, 114111 (2012).

[6] Qingfeng Zhang, Yu Dan, Jian Chen, Yinmei Lu, Tongqing Yang, Xi Yao, Yunbin He, Effects of composition and temperature on energy storage properties of (Pb, La)(Zr, Sn, Ti)O_3 antiferroelectric ceramics, Ceram. Int. 43, 11428 (2017).

[7] Xiaolin Wang, Le Zhang, Xihong Hao, Shengli An, High energy-storage performance of $0.9Pb(Mg_{1/3}Nb_{2/3})O_3$-$0.1PbTiO_3$ relaxor ferroelectric thin films prepared by RF magnetron sputtering, Mater Res Bull. 65, 73 (2015).

[8] Zhenglei Yu, Yunfei Liu, Muyi Shen, Hao Qian, Fangfang Li, Yinong Lyu, Enhanced energy storage properties of $BiAlO_3$ modified $Bi_{0.5}Na_{0.5}TiO_3$-$Bi_{0.5}K_{0.5}TiO_3$ lead-free antiferroelectric ceramics, Ceram. Int. 43, 7653 (2017).

[9] Qingning Li, Changrong Zhou, Jiwen Xu, Ling Yang, Xin Zhang, Weidong Zeng, Changlai Yuan, Guohua Chen, Guanghui Rao, Tailoring antiferroelectricity with

high energy-storage properties in $Bi_{0.5}Na_{0.5}TiO_3$-$BaTiO_3$ ceramics by modulating Bi/Na ratio, J Mater Sci. 27, 10810 (2016).

[10]Ning Xu, Yunfei Liu, Zhenglei Yu, Ruihong Yao, Jiaojiao Ye,Yinong Lu, Enhanced energy storage properties of lead-free (1-x)$Bi_{0.5}Na_{0.5}TiO_3$-x$SrTiO_3$ antiferroelectric ceramics by two-step sintering method, J Mater Sci. 27, 12479 (2016).

[11]Changlai Yuan, Liufang Meng, Yong Liu, Changrong Zhou, Guohua Chen, Qin Feng, Gang Cheng, Guanghui Rao, Microstructures and energy storage properties of Mn-doped 0.97$Bi_{0.47}Na_{0.47}Ba_{0.06}TiO_3-0.03K_{0.5}Na_{0.5}NbO_3$ lead-free antiferroelectric ceramics, J Mater Sci. 26, 8793 (2015).

[12]Ran Xu, Zhuo Xu, Yujun Feng, Hongliang He, Jingjing Tian, Dong Huang, Temperature Dependence of Energy Storage in $Pb_{0.90}La_{0.04}Ba_{0.04}[(Zr_{0.7}Sn_{0.3})_{0.88}Ti_{0.12}]O_3$ Antiferroelectric Ceramics, J. Am. Ceram. Soc. 99, 2984 (2016).

[13]S. Mahajan, O. P. Thakur, K. Sreenivas, C. Prakash, Effect of Nd Doping on Structural,Dielectric and Ferroelectric Properties of $Ba(Zr_{0.05}Ti_{0.95})O_3$ Ceramic, Integr. Ferro. 122, 83 (2010).

[14]Venkata Sreenivas Puli, Dhiren K. Pradhan, Brian C. Riggs, Douglas B. Chrisey, Ram. S. Katiyar, Structure, Ferroelectric, Dielectric and Energy Storage Studies of BaCaTiO, Ba(ZrTi)O Ceramic Capacitors, Integr. Ferro. 157, 139 (2014).

[15]Z. Chen, G.Z. Li, X.J. Sun, L.J. Liu, L. Fang, La_2O_3 modified 0.4$(Ba_{0.8}Ca_{0.2})TiO_3$-0.6$Bi(Mg_{0.5}Ti_{0.5})O_3$ ceramics for high-temperature capacitor applications, Ceram. Int. 41, 11057 (2015).

[16]Y.J. Eoh, E.S. Kim, Dependence of dielectric properties on microstructural characteristics of $(Ba_{0.7}Sr_{0.25}Ca_{0.05})(Ti_{0.9}Zr_{0.1})O_3$ ceramics, Ceram. Int. 41, S2 (2015).

[17]T. Wu, Y.P. Pu, K. Chen, Dielectric relaxation behavior and energy storage properties in $Ba_{0.4}Sr_{0.6}Zr_{0.15}Ti_{0.85}O_3$ ceramics with glass additives, Ceram. Int. 39, 6787 (2013).

[18]S. Xiao, S.M. Xiu, W.Q. Zhang, B. Shen, J.W. Zhai, Y. Zhang, Effects of $Ba_xSr_{1-x}TiO_3$ ceramics additives on structure and energy storage properties of $Ba_{0.4}Sr_{0.6}TiO_3$-BaO-B_2O_3-Al_2O_3-SiO_2 glass-ceramic, J. Alloys Compd. 675, 15 (2016).

[19]Yan Zhang, Yaoyao Li, Haikui Zhu, Zhenxiao Fu, Qitu Zhang, Sintering temperature dependence of dielectric properties and energy-storage properties in $(Ba,Zr)TiO_3$ ceramics, J Mater Sci: Mater Electron. 28, 514 (2017).

[20]Venkata Sreenivas Puli, Ashok Kumar, Douglas B Chrisey, M Tomozawa, J F Scott, Ram S Katiyar, Barium zirconate-titanate/barium calcium-titanate ceramics via sol-gel process:novel high-energy-density capacitors, J. Phys. D:Appl Phys. 44, 395403 (2011).

[21]Zhifu Liu, Zhiqiang Zhang, Faqiang Zhang, Yongxiang Li, Enhanced energy storage properties of barium titanate ceramics made from surface modified particles, J. Adv. Dielect. 3, 1350023 (2013).

[22]Yong Jun Wu, Yu Hui Huang, Nan Wang, Juan Li, Mao Seng Fu, Xiang Ming Chen, Effects of phase constitution and microstructure on energy storage

properties of barium strontium titanate ceramics, J. Eur. Ceram. Soc. 37, 2099 (2017).

[23]Qian Jin, Yong-Ping Pu, Chun Wang, Zi-Yan Gao, Han-Yu Zheng, Enhanced energy storage performance of $Ba_{0.4}Sr_{0.6}TiO_3$ Ceramics:Influence of Sintering Atmosphere, Ceram. Int. 43, S232 (2017).

[24]S. Liu, J.W. Zhai, Improving the dielectric constant and energy density of poly(vinylidene fluoride) composites induced by surface-modified $SrTiO_3$ nanofibers by polyvinylpyrrolidone, J. Mater. Chem. A. 3, 1511 (2015).

[25]G. Zhang, H. Liu, Z. Yao, M. Cao, H. Hao, Effects of Ca doping on the energy storage properties of $(Sr,Ca)TiO_3$ paraelectric ceramics, J Mater Sci: Mater Electron. 26, 2726 (2015).

[26]Zhonghua Yao, Qu Luo, Guifang Zhang, Hua Hao, Minghe Cao, Hanxing Liu, Improved energy-storage performance and breakdown enhancement mechanism of Mg-doped $SrTiO_3$ bulk ceramics for high energy density capacitor applications, J Mater Sci: Mater Electron. 28, 11491 (2017).

[27]Matjaz Spreitzer, Matjaz Valant, Danilo Suvorov, Sodium deficiency in $Na_{0.5}Bi_{0.5}TiO_3$, J. Mater. Chem. 17, 185 (2007).

[28]M. Chandrasekhar, P. Kumar, Synthesis and characterizations of BNT-BT and BNT-BT-KNN ceramics for actuator and energy storage applications, Ceram. Int. 41, 5574 (2015).

[29]Aditya Chauhan, Satyanarayan Patel, Rahul Vaish, Chris R. Bowen, Anti-Ferroelectric Ceramics for High Energy Density Capacitors, Materials. 8,

8009 (2015).

[30]Donggeng Zheng, Ruzhong Zuo, Dongshuai Zhang, Yang Li, Novel $BiFeO_3$-$BaTiO_3$-$Ba(Mg_{1/3}Nb_{2/3})O_3$ Lead-Free Relaxor Ferroelectric Ceramics for Energy-Storage Capacitors, J. Am. Ceram. Soc. 98, 2692 (2015).

[31]N.Triamnak, R.Yimnirun, J.Pokorny, D.P.Cann, Relaxor Characteristics of the Phase Transformation in (1-x)$BaTiO_3$-x$Bi(Zn_{1/2}Ti_{1/2})O_3$ Perovskite Ceramics, J. Am. Ceram. Soc. 96, 3176 (2013).

[32]Z.Yu, C.Ang, R.Guo, A.S.Bhalla, Ferroelectric-relaxor behavior of $Ba(Ti_{0.7}Zr_{0.3})O_3$ ceramics, J. Appl. Phys. 92, 2655 (2002).

[33]S.Kumaragurubaran, T.Nagata, K.Takahashi, S.G.Ri, Y.Tsunekawa, S.Suzuki, T.Chikyow, $BaTiO_3$ based relaxor ferroelectric epitaxial thin-films for high-temperature operational capacitors, J. Appl. Phys. 54, 04DH02 (2015).

[34]Meng Wei, Jihua Zhang, Miaomiao Zhang, Zongying Yao, Hongwei Chen, Chuanren Yang, Relaxor behavior of $BaTiO_3$-$BiYO_3$ Perovskite Materials for high energy density capacitors, Ceram. Int. 43, 4768 (2017).

[35]Tong Wang, Li Jin, Chunchun Li, Qingyuan Hu, Xiaoyong Wei, Relaxor Ferroelectric $BaTiO_3$-$Bi(Mg_{2/3}Nb_{1/3})O_3$ Ceramics for Energy Storage Application, J. Am. Ceram. Soc. 98, 559 (2015).

[36]Longwen Wu, Xiaohui Wang, Longtu Li, Lead-free $BaTiO_3$-$Bi(Zn_{2/3}Nb_{1/3})O_3$ weakly coupled relaxor ferroelectric materials for energy storage, RSC Adv. 6, 14273 (2016).

[37]Xiaobo Zhao, Zhiyong Zhou, Ruihong Liang, Feihua Liu, Xianlin Dong,

High-energy storage performance in lead-free (1-x)$BaTiO_3$-x$Bi(Zn_{0.5}Ti_{0.5})O_3$ relaxor ceramics for temperature stability applications, Ceram. Int. 43, 9060 (2017).

[38]Wen-Bo Li, Di Zhou, Li-Xia Pang, Enhanced energy storage density by inducing defect dipoles in lead free relaxor ferroelectric $BaTiO_3$-based ceramics, Appl. Phys. Lett. 110, 132902 (2017).

[39]Tadej Rojac, Andreja Bencan, Barbara Malic,Goknur Tutuncu, Jacob L. Jones, John E. Daniels, Dragan Damjanovic, $BiFeO_3$ Ceramics:Processing,Electrical, and Electromechanical Properties, J. Am. Ceram. Soc. 97, 1993 (2014).

[40]Donggeng Zheng, Ruzhong Zuo, Enhanced energy storage properties in $La(Mg_{1/2}Ti_{1/2})O_3$-modified $BiFeO_3$-$BaTiO_3$ lead-free relaxor ferroelectric ceramics within a wide temperature range, J. Eur. Ceram. Soc. 37, 413 (2016).

[41]Donggeng Zheng, Ruzhong Zuo, Dongshuai Zhang, Yang Li, Novel $BiFeO_3$-$BaTiO_3$-$Ba(Mg_{1/3}Nb_{2/3})O_3$ Lead-Free Relaxor Ferroelectric Ceramics for Energy-Storage Capacitors, J. Am. Ceram. Soc. 98, 2692 (2015).

[42]F. Wang, C. Leung, Y. Tang, T. Wang, W. Shi, Composition induced structure evolution and large strain response in ternary $Bi_{0.5}Na_{0.5}TiO_3$-$Bi_{0.5}K_{0.5}TiO_3$-$SrTiO_3$ solid solution, J. Appl. Phys. 114, 164105 (2013).

[43]F. Wang, M. Xu, Y. Tang, T. Wang, W. Shi, C.M. Leung, Large Strain Response in the Ternary $Bi_{0.5}Na_{0.5}TiO_3$-$BaTiO_3$-$SrTiO_3$ Solid Solutions, J. Am. Ceram. Soc. 95, 1955 (2012).

[44]M. Kosec, V. Bobnar, M. Hrovat, J. Bernard, B. Malic, J. Holc,New lead-free

relaxors based on the $K_{0.5}Na_{0.5}NbO_3$-$SrTiO_3$ solid solution, J. Mater. Res. 19, 1849 (2004).

[45]Chenwei Cui, Yongping Pu, Ziyan Gao, Jing Wan, Yisong Guo, Chiyuan Hui, Yaru Wang, Yongfei Cui, Structure,dielectric and relaxor properties in lead-free ST-NBT ceramics for high energy storage applications, J. Alloys Compd. 711, 319 (2017).

[46]Haibo Yang, Fei Yan, Ying Lin, Tong Wang, Li He, Fen Wang, A lead free relaxation and high energy storage efficiency ceramics for energy storage applications, J. Alloys Compd. 710, 436 (2017).

[47]Bingyue Qu, Hongliang Du, Zetian Yang, Lead-free relaxor ferroelectric ceramics with high optical transparency and energy storage ability, J. Mater. Chem. C. 4, 1795 (2016).

[48]Zetian Yang, Hongliang Du, Shaobo Qu, Yudong Hou, Hua Ma, Jiafu Wang, Jun Wang, Xiaoyong Wei, Zhuo Xu, Significantly enhanced recoverable energy storage density in potassium-sodium niobate-based lead free ceramics, J. Mater. Chem. A. 4, 13778 (2016).

[49]Tengqiang Shao, Hongliang Du, Hua Ma, Shaobo Qu, Jun Wang, Jiafu Wang, Xiaoyong Wei, Zhuo Xu, Potassium-sodium niobate based lead-free ceramics: novel electrical energy storage materials, J. Mater. Chem. A. 5, 554 (2017).

[50]Qiang Li, Ju Wang, Yuan Ma, Longtao Ma, Guangzhi Dong, Huiqing Fan, Enhanced energy-storage performance and dielectric characterization of $0.94Bi_{0.5}Na_{0.5}TiO_3$-$0.06BaTiO_3$ modified by $CaZrO_3$, J. Alloys Compd. 663, 701

(2016).

[51]Jigong Hao, Zhijun Xu, Ruiqing Chu, Wei Li, Juan Du, Peng Fu, Enhanced energy-storage properties of (1-x)[(1-y)($Bi_{0.5}Na_{0.5}$)TiO_3-y($Bi_{0.5}K_{0.5}$)TiO_3]-x($K_{0.5}Na_{0.5}$)NbO_3 lead-free ceramics, Solid State Commun. 204, 19 (2015).

[52]Qi Xu, Michael T. Lanagan, Xuechen Huang, Juan Xie, Lin Zhang, Hua Hao, Hanxing Liu, Dielectric behavior and impedance spectroscopy in lead-free BNT-BT-NBN perovskite ceramics for energy storage, Ceram. Int. 42, 9728 (2016).

[53]Qingfeng Zhang, Huifen Tong, Jian Chen, Yinmei Lu, Tongqing Yang, Xi Yao, Yunbin He, High recoverable energy density over a wide temperature range in Sr modified (Pb,La)(Zr,Sn,Ti)O_3 antiferroelectric ceramics with an orthorhombic phase, Appl. Phys. Lett. 109, 262901 (2016).

[54]Li Jin, Fei Li, Shujun Zhang, Decoding the Fingerprint of Ferroelectric Loops: Comprehension of the Material Properties and Structures, J. Am. Ceram. Soc. 97, 1 (2014).

[55]W. Y. Pan, C. Q. Dam, Q. M. Zhang, L. E. Cross, Large displacement transducers based on electric field forced phase transitions in the tetragonal ($Pb_{0.97}La_{0.02}$)(Ti,Zr,Sn)O_3 family of ceramics, J. Appl. Phys. 66, 15 (1989).

[56]Ran Xu, Zhuo Xu, Yujun Feng, Xiaoyong Wei, Jingjing Tian, Nonlinear dielectric and discharge properties of $Pb_{0.94}La_{0.04}[(Zr_{0.56}Sn_{0.44})_{0.84}Ti_{0.16}]O_3$ antiferroelectric ceramics, J. Appl. Phys. 120, 144102 (2016).

[57]Wu ZH, Liu HX, Cao MH, Shen ZY, Yao ZH, Hao H, Luo DB, Effect of

BaO-Al_2O_3-B_2O_3-SiO_2 glass additive on densification and dielectric properties of $Ba_{0.3}Sr_{0.7}TiO_3$ ceramics, J. Ceram. Soc. Jpn. 116, 345 (2008).

[58]Young A, Hilmas G, Zhang SC, Schwartz RW, Effect of liquid-phase sintering on the breakdown strength of barium titanate, J Am Ceram Soc. 90, 1504 (2007).

[59]Liebault J, Vallayer J, Goeuriot D, Treheux D, Thevenot F, How the trapping of charges can explain the dielectric breakdown performance of alumina ceramics, J Eur Ceram Soc. 21, 389 (2001).

[60]Huang JJ, ZhangY, Ma T, LiHT, Zhang LW, Correlation between dielectric breakdown strength and interface polarization in barium strontium titanate glass ceramics, Appl. Phys. Lett. 96, 042902 (2010).

[61]Jianxiang Ding, Yunfei Liu, Yinong Lu, Hao Qian, Hong Gao, Hu Chen, Chengjian Ma, Enhanced energy-storage properties of $0.89Bi_{0.5}Na_{0.5}TiO_3$-$0.06BaTiO_3$-$0.05K_{0.5}Na_{0.5}NbO_3$ lead-free anti-ferroelectric ceramics by two-step sintering method, Mater Lett. 114, 107 (2014).

[62]Ning Xu, Yunfei Liu, Zhenglei Yu, Ruihong Yao, Jiaojiao Ye, Yinong Lu, Enhanced energy storage properties of lead-free (1-x)$Bi_{0.5}Na_{0.5}TiO_3$-x$SrTiO_3$ antiferroelectric ceramics by two-step sintering method, J Mater Sci: Mater Electron. 27, 12479 (2016).

[63]Jiaojiao Ye, Yunfei Liu, Yinong Lu, Jianxiang Ding, Chengjian Ma, Hao Qian, Zhenglei Yu, Enhanced energy-storage properties of SrTiO doped (BiNa)TiO-(BiK)TiO lead-free antiferroelectric ceramics, J Mater Sci: Mater Electron. 25, 4632 (2014).

[64]Yongfeng Wang, Zhenlin Lv, Hui Xie, Jing Cao, High energy-storage properties of $[(Bi_{1/2}Na_{1/2})_{0.94}Ba_{0.06}]La_{(1-x)}Zr_xTiO_3$ lead-free anti-ferroelectric ceramics, Ceram. Int. 40, 4323 (2014).

[65]Ye Tian, Li Jin, Hangfeng Zhang, Zhuo Xu, Xiaoyong Wei, E. D. Politova, S. Yu. Stefanovich, Nadezda V. Tarakina, Isaac Abrahams, Haixue Yan, High energy density in silver niobate ceramics, J. Mater. Chem. A. 4, 17279 (2016).

[66]Lei Zhao, Qing Liu, Shujun Zhang, Jing-Feng Li, Lead-free $AgNbO_3$ anti-ferroelectric ceramics with an enhanced energy storage performance using MnO_2 modification, J. Mater. Chem. C. 4, 8380 (2016).

[67]Ye Tian, Li Jin, Hangfeng Zhang, Zhuo Xu, Xiaoyong Wei, Giuseppe Viola, Isaac Abrahams, Haixue Yan, Phase transitions in bismuth-modified silver niobate ceramics for high power energy storage, J. Mater. Chem. A. 5, 17525 (2017).

[68]R. D. Shannon, Acta Crystallogr., Sect. A, Acta Crystallogr. 32, 751 (1976).

[69]Lei Zhao, Qing Liu, Jing Gao, Shujun Zhang, Jing-Feng Li, Lead-Free Antiferroelectric Silver Niobate Tantalate with High Energy Storage Performance, Adv. Mater. 1701824 (2017).

[70]R. D. Shanon, R. X. Fischer, Empirical electronic polarizabilities in oxides, hydroxides, oxyfluorides, and oxychlorides, Phys. Rev. B. 73, 23511 (2006).

[71]Kai Chen, Yongping Pu, Ning Xu, Xu Luo, Effects of $SrO-B_2O_3-SiO_2$ glass additive on densification and energy storage properties of $Ba_{0.4}Sr_{0.6}TiO_3$ ceramics, J Mater Sci: Mater Electron. 23, 1599 (2012).

[72]Xiangrong Wang, Yong Zhang, Xiaozhen Song, Zongbao Yuan, Tao Ma, Qian Zhang, Changsheng Deng, Tongxiang Liang, Glass additive in barium titanate ceramics and its influence on electrical breakdown strength in relation with energy storage properties, J. Eur. Ceram. Soc. 32, 559 (2012).

[73]Yaru Wang, Yongping Pu, Yongfei Cui, Yu Shi, Hanyu Zheng, Enhanced energy storage density of $Ba_{0.4}Sr_{0.6}TiO_3$ ceramics with additive of Bi_2O_3-B_2O_3-ZnO glass, Mater Lett. 201, 203 (2017).

[74]Haibo Yang, Fei Yan, Ge Zhang, Ying Lin, Fen Wang, Dielectric behavior and impedance spectroscopy of lead-free $Ba_{0.85}Ca_{0.15}Zr_{0.1}Ti_{0.9}O_3$ ceramics with B_2O_3 -Al_2O_3-SiO_2 glass-ceramics addition for enhanced energy storage, J. Alloys Compd. 720, 116 (2017).

[75]Tong Wang, Li Jin, Longlong Shu, Qingyuan Hu, Xiaoyong Wei, Energy storage properties in $Ba_{0.4}Sr_{0.6}TiO_3$ ceramics with addition of semi-conductive BaO-B_2O_3-SiO_2-Na_2CO_3-K_2CO_3 glass, J. Alloys Compd. 617, 399 (2014).

[76]Xiaoyong Wei, Haixue Yan, Tong Wang, Qingyuan Hu, G. Viola, Salvatore Grasso, Qinghui Jiang, Li Jin, Zhuo Xu, Michael J. Reece, Reverse boundary layer capacitor model in glass/ceramic composites for energy storage applications, J. Appl. Phys. 113, 024103 (2013).

[77]Yulei Zhang, Weili Li, Wenping Cao, Yu Feng, Yulong Qiao, Tiandong Zhang, Weidong Fei, Mn doping to enhance energy storage performance of lead-free 0.7NBT-0.3ST thin films with weak oxygen vacancies, Appl. Phys. Lett. 110, 243901 (2017).

[78]Sung Sik Won, Masami Kawahara, Lindsay Kuhn, Vineeth Venugopal, J Kwak, Ill Won Kim, Angus I. Kingon, Seung-Hyun Kim, $BiFeO_3$-doped $(K_{0.5},Na_{0.5})(Mn_{0.005},Nb_{0.995})O_3$ ferroelectric thin film capacitors for high energy density storage applications, Appl. Phys. Lett. 110, 152901 (2017).

[79]Zixiong Sun, Chunrui Ma, Xi Wang, Ming Liu, Lu Lu, Ming Wu, Xiaojie Lou, Hong Wang, Chun-Lin Jia, Large Energy Density, Excellent Thermal Stability, and High Cycling Endurance of Lead-Free $BaZr_{0.2}Ti_{0.8}O_3$ Film Capacitors, ACS Appl. Mater. Interfaces. 9, 17096 (2017).

[80]Hao Pan, Yi Zeng, Yang Shen, Yuan-Hua Lin, Jing Ma, Liangliang Li, Ce-Wen Nan, $BiFeO_3$-$SrTiO_3$ thin film as new lead-free relaxor-ferroelectric capacitor with ultrahigh energy storage performance, J. Mater. Chem. A. 5, 5920 (2017).

[81]Biaolin Peng, Qi Zhang, Xing Li, Tieyu Sun, Huiqing Fan, Shanming Ke, Mao Ye, Yu Wang, Wei Lu, Hanben Niu, James F. Scott, Xierong Zeng, Haitao Huang, Giant Electric Energy Density in Epitaxial Lead-Free Thin Films with Coexistence of Ferroelectrics and Antiferroelectrics, Adv Electron Mater. 1, 5 (2015).

[82]X.H.Hao, Z.X.Yue, J.B.Xu, S.L.An, C.W.Nan, Energy-storage performance and electrocaloric effect in (100)-oriented $Pb_{0.97}La_{0.02}(Zr_{0.95}Ti_{0.05})O_3$ antiferroelectric thick films, J. Appl. Phys. 110, 064109 (2011).

[83]Ye Zhao, Xihong Hao, Meiling Li, Dielectric properties and energy-storage performance of $(Na_{0.5}Bi_{0.5})TiO_3$ thick films, J. Alloy. Compd. 601,112 (2014).

[84]Jiaheng Wang, Ningning Sun, Yong Li, Qiwei Zhang, Xihong Hao, Xiujian

Chou, Effects of Mn doping on dielectric properties and energy-storage performance of $Na_{0.5}Bi_{0.5}TiO_3$ thick films, Ceram. Int. 43, 7804 (2017).

[85]Zisheng Xu, Xihong Hao, Shengli An, Dielectric properties and energy-storage performance of $(Na_{0.5}Bi_{0.5})TiO_3$-$SrTiO_3$ thick films derived from polyvinylpyrrolidone-modified chemical solution, J. Alloy. Compd. 639, 387 (2015).

[86]Prateek, Vijay Kumar Thakur, Raju Kumar Gupta, Recent Progress on Ferroelectric Polymer-Based Nanocomposites for High Energy Density Capacitors: Synthesis, Dielectric Properties, and Future Aspects, Chem. Rev. 116, 4260 (2016).

[87]Mahmoud N.Almadhoun, Unnat S.Bhansali, H.N.Alshareef, Nanocomposites of Ferroelectric Polymers with Surface-Hydroxylated $BaTiO_3$ Nanoparticles for Energy Storage Applications, J.Mater.Chem. 22, 11196 (2012).

[88]Lei Gao, Jinliang He, Jun Hu, Yang Li, Large Enhancement in Polarization Response and Energy Storage Properties of Poly(vinylidene fluoride) by Improving the Interface Effect in Nanocomposites, J. Phys. Chem. C. 118, 831 (2014).

[89]Ran Su, Zhengdong Luo, Dawei Zhang, Yang Liu, Zhipeng Wang, Junning Li, Jihong Bian, Yanxi Li, Xinghao Hu, Jinghui Gao, Yaodong Yang, High Energy Density Performance of Polymer Nanocomposites Induced by Designed Formation of $BaTiO_3$@sheet-likeTiO_2 Hybrid Nanofillers, J. Phys. Chem. C. 120, 11769 (2016).

[90]Liyuan Xie, Xingyi Huang, Yanhui Huang, Ke Yang, Pingkai Jiang, Core@Double-Shell Structured $BaTiO_3$-Polymer Nanocomposites with High Dielectric Constant and Low Dielectric Loss for Energy Storage Application, J. Phys. Chem. C. 117, 22525 (2013).

[91]Yu Song, Yang Shen, Penghao Hu, Yuanhua Lin, Ming Li, C. W. Nan, Significant enhancement in energy density of polymer composites induced by dopamine-modified $Ba_{0.6}Sr_{0.4}TiO_3$ nanofibers, Appl. Phys. Lett. 101, 152904 (2012).

[92]Shaohui Liu, Jiwei Zhai, A small loading of surface-modified $Ba_{0.6}Sr_{0.4}TiO_3$ nanofiber-filled nanocomposites with enhanced dielectric constant and energy density, RSC Adv. 4, 40973 (2014).

[93]Shaohui Liu, Jiwei Zhai, Improving the dielectric constant and energy density of poly(vinylidene fluoride) composites induced by surface-modified $SrTiO_3$ nanofibers by polyvinylprrolidone, J. Mater. Chem. A. 3, 1511 (2014).

[94]Haixiong Tang, Henry A. Sodano, Ultra high energy density and fast discharge nanocomposite capacitors, Nano Lett. 13, 1373 (2013).

[95]Zhongbin Pan, Lingmin Yao, Jiwei Zhai, Bo Shen, Haitao Wang, Significantly improved dielectric properties and energy density of polymer nanocomposites via small loaded of $BaTiO_3$ nanotubes, Compos Sci Technol. 147, 30 (2017).

[96]Lingmin Yao, Zhongbin Pan, Shaohui Liu, Jiwei Zhai, Haydn H. D. Chen, Significantly Enhanced Energy Density in Nanocomposite Capacitors Combining the TiO_2 Nanorod Array with Poly(vinylidene fluoride), ACS Appl.

Mater. Interfaces. 8, 26343 (2016).

[97]T. J. Lewis, Interfaces are the dominant feature of dielectrics at the nanometric level, IEEE Trans.Dielectr. Electr. Insul. 11, 739 (2004).

[98]T. Tanaka, M. Kozako, N. Fuse, Y. Ohki, Proposal of a multi-core model for polymer nanocomposite dielectrics, Dielectr. Electr. Insul. 12, 669 (2005).

[99]Xin Zhang, Yang Shen, Qinghua Zhang, Lin Gu, Yuhan Hu, Jiawen Du, Yuanhua Lin, Ce-Wen Nan, Ultrahigh Energy Density of Polymer Nanocomposites Containing $BaTiO_3$@TiO_2 Nanofibers by Atomic-Scale Interface Engineering, Adv. Mater. 27, 819 (2015).

[100]Xiang Lin, Penghao Hu, Zhuye Jia, Shengmin Gao, Enhanced electric displacement induces large energy density in polymer nanocomposites containing core-shell structured $BaTiO_3$@TiO_2 nanofibers, J. Mater. Chem. A. 4, 2314 (2016).

[101]Xin Zhang, Yang Shen, Ben Xu, Qinghua Zhang, Lin Gu, Jianyong Jiang, Jing Ma, Yuanhua Lin, Ce-Wen Nan, Giant Energy Density and Improved Discharge Efficiency of Solution-Processed Polymer Nanocomposites for Dielectric Energy Storage, Adv. Mater. 28, 2055 (2016).

[102]Zhongbin Pan, Lingmin Yao, Jiwei Zhai, Bo Shen, Shaohui Liu, Haitao Wang, Jinhua Liu, Excellent energy density of polymer nanocomposites containing $BaTiO_3$@Al_2O_3 nanofibers induced by moderate interfacial area, J. Mater. Chem. A. 4, 13259 (2016).

[103]P. Hu, J. Wang, Y. Shen, Y. Guan, Y. Lin, C.-W. Nan, Highly enhanced energy

density induced by hetero-interface in sandwich-structured polymer nanocomposites, J. Mater. Chem. A. 1, 12321 (2013).

[104]P. Hu, Y. Shen, Y. Guan, X. Zhang, Y. Lin, Q. Zhang, C.-W. Nan, Topological-Structure Modulated Polymer Nanocomposites Exhibiting Highly Enhanced Dielectric Strength and Energy Density, Adv. Funct. Mater. 24, 3172 (2014).

[105]L. L. Sun, B. Li, Y. Zhao, G. Mitchell, W. H. Zhong, Structure-induced high dielectric constant and low loss of CNF/PVDF composites with heterogeneous CNF distribution, Nanotechnology. 21, 305702 (2010).

[106]Hang Luo, Dou Zhang, Lu Wang, Chao Chen, Jing Zhou, Kechao Zhou, Highly enhanced dielectric strength and energy storage density in hydantoin@$BaTiO_3$-P(VDF-HFP) composites by a sandwich-structure, RSC Adv. 5, 52809 (2015).

[107]Yifei Wang, Jin Cui, Linxi Wang, Qibin Yuan, Yujuan Niu, Jie Chen, Qing Wang, Hong Wang, Compositional Tailoring Effect on Electric Field Distribution for Significantly Enhanced Breakdown Strength and Restrained Conductive Loss in Sandwich-Structured Ceramic/Polymer Nanocomposites, J. Mater. Chem. A. 5, 4710 (2017).

[108]Zhongbin Pan, Baihui Liu, Jiwei Zhai, Lingmin Yao, Ke Yang, Bo Shen, $NaNbO_3$ Two-Dimensional Platelets Induced Highly Energy Storage Density in Trilayered Architecture Composites, Nano Energy. 40, 587 (2017).

[109]Yang Shen, Dashan Shen, Xin Zhang, Jianyong Jiang, Zhenkang Dan, Yu Song,

Yuanhua Lin, Ming Li, Ce-Wen Nan, High Energy Density of Polymer Nanocomposites at Low Electric Field induced by Modulation of Topological-Structure, J.Mater.Chem.A. 4, 8359 (2016).

[110]Zhong-Hui Shen, Jian-Jun Wang, Yuanhua Lin, Ce-Wen Nan, Long-Qing Chen, Yang Shen, High-Throughput Phase-Field Design of High-Energy-Density Polymer Nanocomposites, Adv. Mater. 1704380 (2017).

[111]Feihua Liu, Qi Li, Jin Cui, Zeyu Li, Guang Yang, Yang Liu, Lijie Dong, Chuanxi Xiong, Hong Wang, Qing Wang, Nanocomposites: High-Energy-Density Dielectric Polymer Nanocomposites with Trilayered Architecture, Adv. Funct. Mater. 27, 1606292 (2017).

[112]X. F. Chen, H. L. Zhang, F. Cao, G. S. Wang, X. L. Dong, Y. Gu, H. L.He, Y. S. Liu, Charge-discharge properties of lead zirconate stannate titanate ceramics, J. Appl. Phys. 106, 034105 (2009).